Modeling the effects of slip, twinning, and notch on the deformation of single-crystal austenitic manganese steel

S. Virupakshi [a] , X. Zheng [b], K. Frydrych [a], I. Karaman [b], A. Srivastava [b],
K. Kowalczyk-Gajewska [a],*

[a] *Institute of Fundamental Technological Research, Polish Academy of Sciences, Pawińskiego 5B, 02-106 Warsaw, Poland*
[b] *Department of Materials Science & Engineering, Texas A&M University, College Station, TX 77843, USA*

ARTICLE INFO

ABSTRACT

The objective of this work is to deconvolute the interaction of slip, twinning, and notch on the deformation response of an austenitic manganese (Hadfield) steel using detailed finite element simulations. The simulations employ a rate-dependent crystal plasticity constitutive model that incorporates both slip and twinning deformation mechanisms. The model accounts for the spatially non-uniform appearance of new twin-related orientations, hardening due to slip–twin interactions, and modified properties of the twinned crystal. Limited experiments on single-crystal dog-bone and single-edge notch specimens, with two crystal orientations, are also conducted to aid the simulation. Several features of the experimental observations are accurately captured in the simulations. For example, simulations accurately capture distinct stress–strain responses associated with different crystallographic orientations, including variations in initial hardening behavior followed by either decreasing or increasing hardening depending on the dominant deformation mechanisms. The simulation also captures the observed orientation-dependent asymmetric deformation of the notch in single-edge notch specimens. Additionally, by selectively activating deformation mechanisms, the role of twinning is isolated and its influence on both global and local response is clearly demonstrated. These results provide a mechanistic understanding of how deformation mode interactions and local geometry (i.e., notch) influence the response of these materials.

1. Introduction

Austenitic manganese steels, known as Hadfield steels, are characterized by their high strain-hardening rate, exceptional ductility, toughness, and wear resistance, and are widely employed in applications such as railroads, heavy machinery, and armored vehicles (Subramanyam et al., 1990; Havlíček and Bušová, 2012; Havel, 2017; Okechukwu et al., 2018). Their remarkable mechanical behavior is primarily attributed to the activation of deformation twinning, which has been experimentally studied using mechanical testing of both polycrystalline (Raghavan et al., 1969; Dastur and Leslie, 1981; Adler et al., 1986; Hutchinson and Ridley, 2006; Bayraktar et al., 2004) and single crystal specimens (Karaman et al., 2000a, 2001a, 1998, 2000b; Efstathiou and Sehitoglu, 2010; Canadinc et al., 2007; Zheng et al., 2025). Twinning activity has also been recognized as an important factor influencing deformation and failure in other manganese steels; see for example (Ding et al., 2024; Shen et al., 2024).

Specifically, in the recent in-situ experimental work by Zheng et al. (2025), the deformation and fracture behavior of austenitic manganese steels was studied using both single-crystal dog-bone and single-edge notch tension specimens. These experiments showed

---

that, in austenitic manganese steels, twinning continues to evolve with increasing deformation, and both twinned and untwinned regions undergo significant plastic deformation. Importantly, these experiments showed that, in a single-edge notch specimen oriented for twinning as the dominant deformation mechanism, the initially symmetrical notch undergoes large asymmetrical deformation. With continued deformation, multiple microcracks nucleate at the intersections of the deformed notch and twin boundaries. In contrast, in single-edge notch specimens oriented for crystallographic slip as the dominant deformation mechanism, the notch deforms symmetrically, with a single crack eventually nucleating from the center of the deformed notch.

While these experiments provide valuable insight, to the best of our knowledge, there is currently no work on modeling the effects of slip, twinning, and notch on the deformation of austenitic manganese steels. Existing crystal plasticity finite element (CPFE)-based modeling studies on notched specimens have mainly focused on other single- or polycrystalline metals and have rarely incorporated deformation twinning. For example, Selvarajou et al. (2016) investigated the micromechanics of anisotropic plastic flow via combined slip and twinning in single crystals, and Baweja and Joshi (2024) modeled polycrystalline circular-notched specimens of magnesium. Similarly, Prasad et al. (2017) performed plane strain simulations of cylindrical void growth ahead of a notch tip in magnesium single crystals. More recently, Sahu et al. (2024) examined single V-notch CP-Ti polycrystals both experimentally and through CPFE simulations, but their modeling was restricted to the notch region, which was treated as a second-phase material with very low stiffness, and twinning was neglected. Furthermore, the interaction of twinning and notch in austenitic manganese steels is unlike that in magnesium or its alloys and other quasi-brittle materials, where twin boundaries serve as weak interfaces or discontinuities in the absence of significant plastic deformation, simply providing a pathway for crack growth (Kaushik et al., 2014a,b).

Following these, the objective of this work is to deconvolute the effects of slip and twinning on the deformation response of both dog-bone (which induces uniaxial loading) and single-edge notch (which induces more complex multiaxial loading) tension specimens using detailed CPFE simulations. These simulations allow us to selectively introduce deformation mechanisms, enabling a clear evaluation of their individual roles. Furthermore, there is always variability in experiments, such as the orientation of the single-crystal specimens. As such, parametric studies are also carried out to understand the effect of these misorientations. To aid these simulations, limited experiments on both single-crystal dog-bone and single-edge notch tension specimens of Hadfield steels, with axes aligned close to ⟨001⟩ or ⟨111⟩, have also been conducted.

The FE simulations carried out herein involve modeling large deformations in three-dimensional dog-bone and single-edge notch tension specimens using a continuum rate-dependent crystal plasticity constitutive model with deformation twinning. For FCC austenitic manganese steels, there are twelve possible slip systems and twelve possible twin systems, all of which are considered in this work. The constitutive model with twinning accounts for three main effects: (i) crystal reorientation (Tomé et al., 1991; Staroselsky and Anand, 1998; Kowalczyk-Gajewska, 2013), (ii) hardening with latent directional effects from slip–twin interactions (Karaman et al., 2000a; Proust et al., 2007), and (iii) modified properties for the crystal formed after reorientation (Frydrych et al., 2020). A key novelty of the present approach is the detailed treatment of the third aspect.

There are numerical challenges in incorporating twin-related reorientation in the CPFE method. In particular, when twinning criteria are met at a material point, a new crystal orientation must be assigned, which can lead to numerical instabilities. Typically, a mean-field two-phase model by Kalidindi (2001) is used until the twin volume fraction reaches a critical value, often around 0.9, at which point the crystal is reoriented and no longer deforms by twinning (Zhang and Joshi, 2012; Liu and Wei, 2014), resulting in smooth stress and strain fields that contradict experimental observations. In this work, we use a probabilistic twin-volume-consistent scheme (Kowalczyk-Gajewska, 2011), allowing parent and twinned orientations to coexist within the twinning domain and accounting for the volume effect of twins in the simulations. The CPFE implementation, together with the reorientation scheme, is performed using the AceGen package—a tool of automatic differentiation enabling us to obtain the consistent tangent operator and computationally efficient code (Korelc, 2002). Moreover, a few techniques recently proposed in the literature (Dittmann and Wulfinghoff, 2023; Mànik et al., 2022; Korelc and Stupkiewicz, 2014) have been combined to further enhance the computational efficiency of the framework.

We note that there are several approaches to modeling of deformation twinning, such as the phase-field method, which not only accounts for the nucleation and evolution of twins but also their morphology (Rezaee-Hajidehi et al., 2022; Mo et al., 2022; Liu et al., 2023). Additional approaches include incorporating the twin evolution law into the constitutive description (Qiao et al., 2016; Cheng et al., 2018), using post-remeshing tools to explicitly introduce twins within the grains (Ardeljan et al., 2015), or modifying the single-crystal energy function by adding an interaction energy term to penalize the simultaneous existence of the matrix and the twin (Chester et al., 2016; Huang et al., 2022). However, these methods require knowledge of additional parameters and are extremely computationally expensive. As such, modeling the full three-dimensional specimen with all possible slip and twin systems – which is necessary to simulate the response of a single-edge notch specimen – is practically unrealistic. There are also formulations that account for twinning–detwinning effects (Wang et al., 2013), which have been extended and applied in the context of the mean-field elastic–viscoplastic self-consistent model (Qiao et al., 2017; Cheng et al., 2024) and implemented in the FE method (Yaghoobi et al., 2022). Temperature effects have also been incorporated (Hollenweger and Kochmann, 2022) into the variational CP framework (Chang and Kochmann, 2015). However, since cyclic loading and temperature effects are not the focus of our work, the complexity of the proposed approach is considered sufficient in the present context, leading to a computationally efficient numerical implementation.

Our results show that the CPFE simulations using a fully calibrated constitutive model accurately capture the deformation response of both ⟨001⟩-oriented (which preferentially activates slip) and ⟨111⟩-oriented (which preferentially activates twinning) single-crystal dog-bone specimens of austenitic manganese steel. The simulations also capture the relative differences in the response of ⟨001⟩- and ⟨111⟩-oriented single-edge notch specimens, as well as accurately predict the differences in the local deformation of

the notches in these specimens. Furthermore, by selectively activating slip and twinning in the simulations, we clearly evaluate their individual roles. We also assess the impact of differences in the orientation of the single-crystal specimens on the interaction of slip, twinning, and the notch in the deformation behavior of single-crystal austenitic manganese steel. The remainder of the paper is organized as follows: a brief description of the experiments is provided in Section 2, the numerical method is detailed in Section 3, the results and discussion are presented in Section 4, and the conclusions are drawn in Section 5.

2. Experimental method

The material used in this work is single crystals of Hadfield steel with a nominal composition of 13 wt% manganese, 1.1 wt% carbon, and the remainder being iron, as in Zheng et al. (2025) and other experimental works (Karaman et al., 1998, 2000a,b, 2001a). The single crystals were grown using the Bridgman technique in a helium atmosphere, with the crystal growth direction approximately aligned along either the ⟨001⟩ or ⟨111⟩ crystallographic orientations. These crystals were then subjected to homogenization heat treatment at 1373 K for 24 h in an inert gas atmosphere. Subsequently, flat dog-bone specimens with a gauge length of approximately 8 mm, a width of approximately 3 mm, and a thickness of approximately 0.7 mm, aligned along the crystal growth direction, were machined using wire electrical discharge machining. After machining, the specimens were solutionized at 1373 K for 1 h and then quenched in water at room temperature. All solutionized single-crystal specimens exhibited single-phase austenite without retained carbides or second phases (Zheng et al., 2025; Karaman et al., 1998, 2000a,b, 2001a), consistent with broader studies on high-Mn austenitic steels showing that solution annealing fully dissolves carbides in alloys with carbon contents near 1 wt% (as in Hadfield steel), yielding a homogeneous single-phase austenite (Gürol and Kurnaz, 2020).

In a subset of flat dog-bone specimens, a notch approximately 1.5 mm long with a root radius of approximately 45 μm was machined across the gauge width in the middle of the gauge section using a diamond wire saw. All the mechanical tests were performed using a miniature tension/compression module (Kammrath & Weiss) under a high-resolution digital optical microscope (Olympus DSX510), which allowed us to capture images of the deforming sample. This was particularly important for capturing the local deformation of the notch in single-edge notch specimens.

Under the monotonic room-temperature loading considered here, long-range diffusion of Mn and C is minimal; accordingly, we assume a chemically homogeneous austenite and do not consider solute segregation to interfaces. This is consistent with observations in Fe–Mn–C austenitic steels that deformation-induced (coherent) twin boundaries exhibit negligible segregation compared with non-coherent/high-angle grain boundaries (Herbig et al., 2015).

In Zheng et al. (2025), where the primary focus was on ⟨111⟩-oriented single crystals of Hadfield steel, extensive experimental analysis of deformation-induced microstructure evolution was carried out using ex-situ and in-situ scanning electron microscopy (SEM) and electron backscattered diffraction (EBSD) analysis. Additionally, fractographic analysis of the fracture specimens was conducted using SEM imaging. Detailed analysis of twin formation and their structure in Hadfield steel has also been carried out extensively using transmission electron microscopy (TEM) in Karaman et al. (1998, 2000a,b) and Karaman et al. (2001a). These results are discussed in the context of the current modeling results wherever relevant.

3. Numerical method

The effects of crystallographic slip, twinning, and the presence of a notch in single-crystal austenitic manganese steel are analyzed using three-dimensional finite deformation FE simulations of dog-bone and single-edge notch tension specimens. These simulations employ a continuum rate-dependent crystal plasticity constitutive model that accounts for deformation twinning. The crystal plasticity constitutive model and the FE implementation are described below.

3.1. Crystal plasticity constitutive model

The crystal plasticity constitutive model used to carry out FE simulations of FCC single crystals deforming by slip and twinning follows from the work of Kowalczyk-Gajewska (2010). However, in that prior work, the model was formulated in a velocity-based framework, neglecting elastic strains, and was combined with mean-field models of polycrystals: the iso-strain Taylor approach and the VPSC model (Lebensohn and Tomé, 1993). In this work, the model has been adapted for incorporation into CPFE method.

We consider the elastic-viscoplastic model of a single crystal formulated in a displacement-based framework, and the kinematic description follows standard formulations (Hill and Rice, 1972; Asaro and Needleman, 1985). The deformation gradient $\mathbf{F}$ is multiplicatively decomposed into two parts:

$$\mathbf{F} = \mathbf{F}_e \mathbf{F}_p \tag{1}$$

where $\mathbf{F}_e$ and $\mathbf{F}_p$ denote the elastic and plastic components, respectively. The evolution of the plastic part of the deformation gradient is governed by the equations:

$$\dot{\mathbf{F}}_p = \hat{\mathbf{L}}_p \mathbf{F}_p, \tag{2}$$

where the dot over the quantity denotes its material time derivative.

Table 1
Slip and twin systems in FCC austenitic manganese steel considered in this work.

	Slip/Twin plane	Slip/Twin direction	Number of systems
Slip	{111}	$\langle \bar{1}10 \rangle$	12
Twinning	{111}	$\langle 211 \rangle$	12

The usual approach (Chin et al., 1969; Kalidindi, 1998, 2001; Staroselsky and Anand, 1998, 2003) is used to account for twinning in the crystal plasticity model. Twinning is considered as a pseudo unidirectional slip mode. The rate of pseudo slip $\dot{\gamma}^l_{(t)}$ is related to the rate of volume fraction $\dot{f}^l$ of the twinned part formed by the twin system l as

$$\dot{\gamma}^l_{(t)} = \gamma^{TW} \dot{f}^l, \tag{3}$$

where $\gamma^{TW} (= 1/\sqrt{2}$ for FCC crystal) is the characteristic twin shear strain. Denoting by $\dot{\gamma}^k_{(s)}$ as the rate of slip on the kth slip system, the plastic part of the velocity gradient $\hat{\mathbf{L}}_p$ is described as follows:

$$\hat{\mathbf{L}}_p = \sum_{k=1}^{2M} \dot{\gamma}^k_{(s)} \mathbf{m}^k_0 \otimes \mathbf{n}^k_0 + \sum_{l=1}^{N} \dot{\gamma}^l_{(t)} \mathbf{m}^l_0 \otimes \mathbf{n}^l_0 = \sum_{r=1}^{2M+N} \dot{\gamma}^r \mathbf{m}^r_0 \otimes \mathbf{n}^r_0, \tag{4}$$

where $\mathbf{m}^r_0$ and $\mathbf{n}^r_0$ are the unit vectors along the slip/twin direction and normal to the slip/twin plane of the system r in the reference configuration, M denotes the number of slip systems and N the number of twinning systems, respectively; see Table 1.

To unify the description of slip and twinning in Eq. (4), the slip in the $\mathbf{m}$ direction is distinguished from the slip in the $\bar{\mathbf{m}}$ direction, and $\dot{\gamma}^r (\geq 0)$ denotes the magnitude of shear rate in the rth deformation mode.

The rate of shearing on a given slip or twinning system r is calculated using the visco-plastic power law (Asaro and Needleman, 1985):

$$\dot{\gamma}^r = \dot{\gamma}_0 \left(\frac{\tau^r}{\tau^r_c} \right)^n, \tag{5}$$

where $\dot{\gamma}_0$ is the reference shear rate, n is the strain-rate-sensitivity exponent, τ^r is a non-negative resolved shear stress and τ^r_c its critical value. The resolved shear stress is defined by the projection of the Mandel stress tensor $\mathbf{M}_e$ on the plane of slip $\mathbf{n}^r_0$ and in the direction $\mathbf{m}^r_0$:

$$\tau^r = \langle \mathbf{m}^r_0 \cdot \mathbf{M}_e \cdot \mathbf{n}^r_0 \rangle \geq 0, \quad \mathbf{M}_e = \mathbf{F}^T_e \mathbf{S} \mathbf{F}^T_p = \mathbf{F}^T_e \boldsymbol{\tau} \mathbf{F}^{-T}_e, \tag{6}$$

where $\langle \cdot \rangle \equiv \frac{1}{2}((\cdot) + | \cdot |)$, $\mathbf{S}$ is the first Piola–Kirchhoff stress and $\boldsymbol{\tau}$ is the Kirchhoff stress. The Mandel stress tensor is obtained using a hyper-elastic law:

$$\mathbf{M}_e = 2\mathbf{C}_e \frac{\partial \Psi}{\partial \mathbf{C}_e}, \tag{7}$$

where $\mathbf{C}_e = \mathbf{F}^T_e \mathbf{F}_e$ is the right elastic Cauchy–Green tensor and

$$\Psi = \frac{1}{2} \mathbf{E}_e \cdot \mathbb{L}^e \cdot \mathbf{E}_e \tag{8}$$

is the Kirchhoff-type function of free energy density per unit volume in the reference configuration, $\mathbb{L}^e$ is the anisotropic stiffness tensor of single crystal and $\mathbf{E}_e = \frac{1}{2}(\mathbf{C}_e - \mathbf{1})$ is the elastic Lagrangian strain tensor.

The critical resolved shear stress τ^r_c evolves differently with accumulated slip and accumulated twin volume fraction according to the hardening laws (Kowalczyk-Gajewska, 2010, 2011) developed based on prior experimental observations (Kalidindi, 2001; Szczerba et al., 2004; Karaman et al., 2000a, 2001b; Sahoo et al., 2019, 2020).

Hardening of slip systems due to slip and twinning activity is described as follows:

$$\dot{\tau}^r_c = \dot{\tau}^{r+M}_c = H^r_{(ss)} \sum_{q=1}^{M} h^{(ss)}_{rq} \dot{\hat{\gamma}}^q + H^r_{(st)} \sum_{q=2M+1}^{2M+N} h^{(st)}_{rq} \dot{\gamma}^q \quad (r \leq M), \tag{9}$$

where $\dot{\hat{\gamma}}^q = \dot{\gamma}^q + \dot{\gamma}^{q+M}$. The latent hardening on a given system r due to activity on system q is described using the submatrices $h^{(\alpha\beta)}_{rq} = q^{(\alpha\beta)} + (1 - q^{(\alpha\beta)})|\mathbf{n}^r \cdot \mathbf{n}^q|$, where $q^{(\alpha\beta)}$ $(\alpha, \beta = t, s)$ are the latent hardening parameters and the term $|\mathbf{n}^r \cdot \mathbf{n}^q|$ is responsible for considering the influence of coplanarity of systems. $H^r_{(ss)}$ and $H^r_{(st)}$ denote hardening moduli of slip systems due to slip and twinning activity,

$$H^r_{(ss)} = h^{ss}_1 + h^{ss}_0 \exp \left(\frac{-h^{ss}_0}{\tau^{ss}_{sat}} \Gamma^s \right), \quad H^r_{(st)} = h^{st}_0 \left(\frac{f^{TW}}{f^{st}_{sat} - f^{TW}} \right) \tag{10}$$

with

$$\Gamma^s = \int \dot{\Gamma} \mathrm{d}t, \quad \dot{\Gamma} = \sum_{r=1}^{M} \dot{\hat{\gamma}}^r, \tag{11}$$

where $h_0^{ss}, h_1^{ss}, h_0^{st}, \tau_{sat}^{ss}$ and f_{sat}^{st} are hardening parameters and f^{TW} is the total volume fraction of twins.

On the other hand, hardening of twin systems due to slip and twinning activity is specified as follows:

$$\dot{\tau}_c^r = H_{(ts)}^r \sum_{q=1}^{M} h_{rq}^{(ts)} \dot{\gamma}^q + H_{(tt)}^r \sum_{q=2M+1}^{2M+N} h_{rq}^{(tt)} \dot{\gamma}^q \quad (r > 2M). \tag{12}$$

$H_{(ts)}^r$ and $H_{(tt)}^r$ denote hardening moduli of twin systems due to slip and twinning activity and are specified as

$$H_{(ts)}^r = h_1^{ts} + h_0^{ts} \exp\left(\frac{-h_0^{ts}}{\tau_{sat}^{ts}} \Gamma^s\right), \quad H_{(tt)}^r = \frac{h_0^{tt}}{\gamma^{TW}} \left(\frac{f^{TW}}{f_{sat}^{tt} - f^{TW}}\right) \tag{13}$$

Similarly, as in Eq. (10), $h_0^{ts}, h_1^{ts}, h_0^{tt}, \tau_{sat}^{ts}$ and f_{sat}^{tt} are hardening parameters to be identified for the material of interest.

In the present study, in order to reduce the number of parameters, hardening of slip due to twinning is neglected ($H_{(st)}^r = 0$) and the latent hardening coefficient $q^{(ss)} = 1$. Moreover, hardening of twin due to slip is specified solely by the linear term in Eq. (13)$_1$, so that $h_0^{(ts)} = 0$ (τ_{sat}^{ts} is then redundant), and the latent hardening coefficients $q^{(ts)} = q^{(tt)} = 1$. Some remarks on the influence of the $q^{(\alpha\beta)}$ value are included in Appendix B. An extensive discussion on the physical nature of latent hardening for slip–twin interactions can be found in El Kadiri and Oppedal (2010).

In the event that the reorientation condition is true for a given point, and the crystal lattice at this point has been reoriented due to twinning, the newly formed crystal is assumed to be described by the same material model, but with different material parameters. This accounts for the fact that the mechanical characteristics of twins differ from those of the parent crystal mainly due to Basinski's mechanism, i.e., the change of glissile dislocations into sessile ones (Sahoo et al., 2019). Secondary twinning is more difficult to initiate than slip in twinned regions. This is because twinning evolution in Hadfield steel is usually observed in the form of multiple thin layers (Zheng et al., 2025), which eventually join rather than the growth of a single twin as in magnesium. Thus, in the present calculations, we assumed that twinning is no longer possible in reoriented regions, while the initial critical shear stress τ_c^0 for slip and the hardening parameters h_0^{ss}, h_1^{ss}, and τ_{sat}^{ss} are modified.

The probabilistic twin volume consistent (PTVC) reorientation scheme (Kowalczyk-Gajewska, 2010, 2013) is applied to account for lattice reorientation due to twinning. It ensures that the twin volume fraction and the proportion of reoriented domains in the sample are consistent. When the reorientation criterion is met, a crystal lattice is reoriented to twin-related orientation. It should be emphasized that information accessible at the given material point (i.e., Gauss point in FE mesh) is sufficient to validate this reorientation criterion and that at the current deformation step a one-phase material (single orientation) is assumed to exist at this point. The condition is as follows:

$$\text{if} \quad (\Delta f^{TW} > \xi \quad \text{and} \quad f^{TW} > f_0^{crit}) \quad \text{or} \quad f^{TW} > f^{crit} \quad \rightarrow \quad \mathbf{a}^{new} = \mathbf{R}^{TW} \mathbf{a}^{old}$$

where Δf^{TW} is the increment of twin volume for a given time step, ξ is a number randomly generated from the set $(0, \Psi_t)$ and $\Psi_t = 1 - (f^{TW} - \Delta f^{TW})$, while f^{crit} is a value of twin volume fraction for which the reorientation is always performed. The condition is checked once the volume fraction of twin exceeds f_0^{crit}. $\mathbf{R}^{TW}$ is the rotation tensor

$$\mathbf{R}^{TW} = 2\mathbf{n}^{TW} \otimes \mathbf{n}^{TW} - \mathbf{I} \tag{14}$$

where $\mathbf{n}^{TW}$ is a unit normal to the twin plane of the twin system l for which $\gamma^l = \gamma^{TW} f^l$ is maximum at the given time step. $\mathbf{R}^{TW}$ rotates any crystallographic direction $\mathbf{a}^{old}$ of the parent orientation to the corresponding $\mathbf{a}^{new}$ of the twin-related one. It must be emphasized that the condition is probabilistic in its nature, so, in general, formation of the twin-matrix laminate or distinct twin lamellas is not observed in the calculations. However, parent and twinned orientations co-exist within the FE mesh within the domains of twinning activity, enabling one to account for the volume effect of twins in the simulations.

The present crystal plasticity formulation does not incorporate size effects. Such effects could be included by introducing length-scale parameters, for example, through a size-dependent initial critical stress (Meyers et al., 2001; Wong et al., 2016) or by making certain hardening parameters proportional to the mean free path for dislocations or the characteristic width of twin platelets (Karaman et al., 2001b). Since samples of the same material but with significantly different dimensions were not studied, this extension is not relevant in the present context.

In the current formulation, twinning and detwinning are disabled after reorientation at a given Gauss point to improve computational efficiency. This assumption is not expected to affect the results, as the loading processes considered are nominally proportional, and strain or stress reversal – required for detwinning (Wang et al., 2013; Yaghoobi et al., 2020; Frydrych et al., 2021) – is unlikely. Nevertheless, the model and the PTVC reorientation scheme can account for detwinning or multiple twinning–detwinning events if the post-reorientation grain description allows twinning. In that case, the reorientation scheme operates as for the parent grain, with the rotation tensor in Eq. (14) defined by the unit normal to the twin plane corresponding to the system with the maximum accumulated twin volume fraction since the last reorientation. The hardening moduli $H_{(st)}$ and $H_{(tt)}$ in Eqs. (10) and (13) are then determined from the total twin volume fraction accumulated over the same period.

The constitutive model also does not track solute redistribution or segregation to twin boundaries. This simplification is appropriate for the present solutionized single-crystal Hadfield steel tested under monotonic loading (see Section 2), where deformation-induced twins are expected to show little or no segregation (Herbig et al., 2015). However, in other loading histories or environments (e.g., hydrogen charging) or in other material systems, segregation at twin boundaries can occur and may influence the deformation mechanisms. Extending the framework to include chemo–mechanical coupling represents an interesting direction for future work.
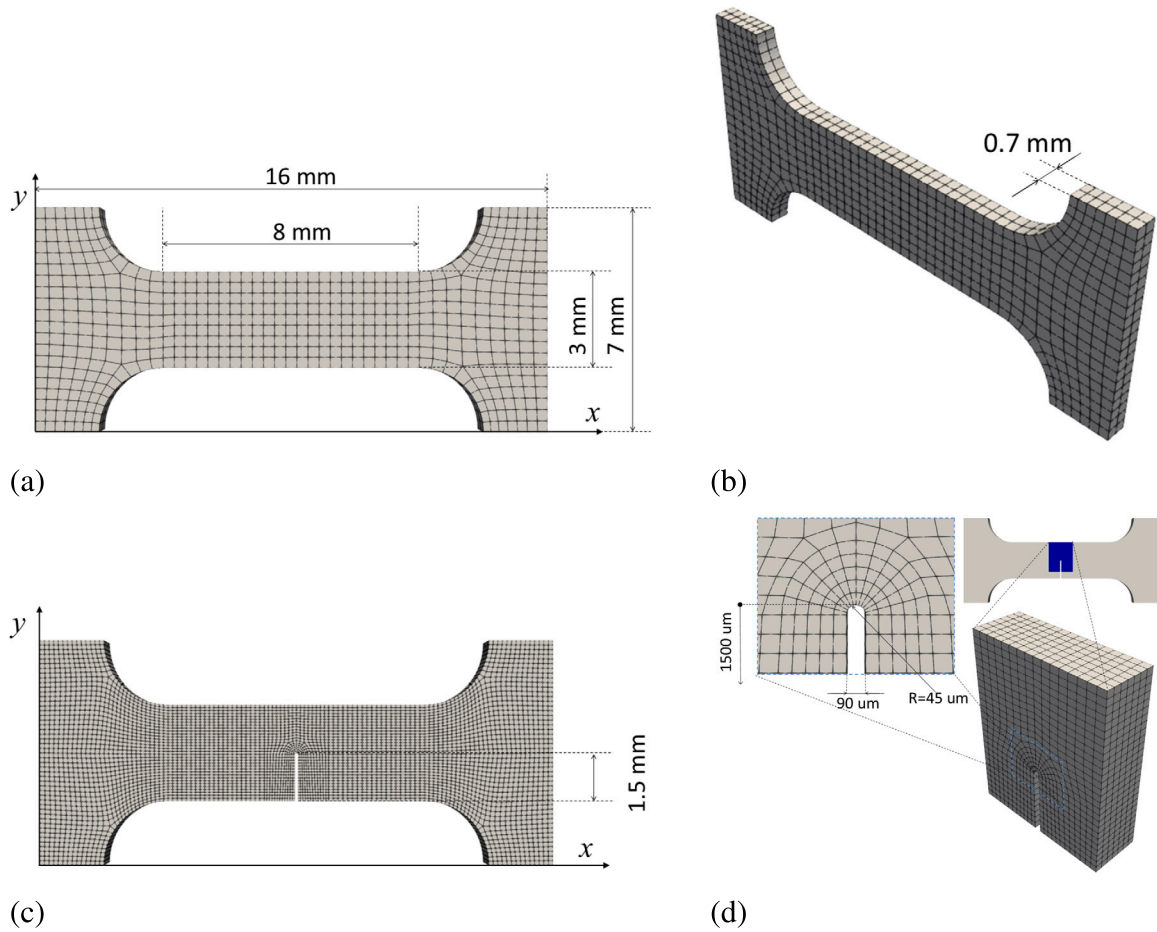
Fig. 1. Geometry and FE mesh of the specimens: (a)–(b) flat dog-bone and (c) single-edge notch with (d) zoomed-in view of the notch region.

3.2. Finite element model

The full geometry of both dog-bone and single-edge notch specimens, with the same dimensions as in the experiments (Section 2), is modeled for CPFE simulations. The modeled geometry of these specimens along with the FE mesh is shown in Fig. 1. Modeling the full geometry of the specimen is essential in this case to account for the boundary conditions imposed in the experiments and to avoid over- or under-constraining the material deformation. The FE mesh for all specimens employs 20-noded brick elements. Since the present CPFE model does not include any intrinsic size effects, the simulated response is invariant to proportional scaling of the sample geometry. The absolute dimensions used in the simulations are therefore chosen to match the single-crystal specimens tested experimentally, and the material parameters are calibrated using those data. Consequently, the calibrated parameters are valid for specimens of similar dimensions and loading conditions.

The FE discretization of the dog-bone and single-edge notch specimens differs, as the presence of a notch is expected to lead to localized deformation in its vicinity. Accordingly, an approximately 2.5-times denser mesh is used for single-edge notch specimens compared to dog-bone specimens, with additional refinement around the notch area. The mesh densities for both specimen types are determined based on a standard mesh sensitivity study. Selected results from this study, related to the robustness of the PTVC scheme, are included in Appendix A.

For both specimen types, two main sets of crystal orientations are considered: one where the specimen axis is aligned with the [001] crystallographic direction, and another where it is aligned with or close to [111]. For the [111] orientation, parametric studies are also carried out to understand the effect of deviations from the exact [111] orientation. All orientation instances considered here are listed in Table 2. Orientation [111]Exp corresponds to the one measured in the experiment; see also Zheng et al. (2025). The orientation is misoriented with respect to the ideal orientation [111], both in terms of the loading axis and the sample plane. The loading axis is slightly misoriented with the $[\bar{1}\bar{1}1]$ direction (symmetrically equivalent to [111]), while the sample plane is not perfectly aligned with the crystal plane $[\bar{1}0\bar{1}]$ (symmetrically equivalent to $[1\bar{1}0]$). This means that the sample plane is not a symmetry plane of the crystal. The total misorientation angle is approximately 6°. Orientations [111]A and [111]B are obtained by rotating

Table 2

Crystal orientation instances considered in simulations with the respective global coordinate axes. Note that the loading directions for orientation [111]Exp, and directions x and y for [111]A and [111]B, are given by the coordinates of the respective sample basis vectors in the crystal frame, while Miller indices are used in the remaining cases.

Case	Primary loading direction (x)	Lateral direction (y)	Lateral direction (z)	Euler angles
Orientation [001]	[001]	[110]	[$\bar{1}$10]	$\{225°, 90°, 90°\}$
Orientation [111]	[111]	[11$\bar{2}$]	[$\bar{1}$10]	$\{225°, 90°, 144.74°\}$
Orientation [111]Exp	[$-0.56, -0.59, 0.59$]	[$-0.48, 0.81, 0.33$]	[$-0.67, -0.096, -0.73$]	$\{278.16°, 137.36°, 60.47°\}$
Orientation [111]A	[0.62, 0.62, 0.49]	[0.34, 0.34, -0.87]	[$\bar{1}$10]	$\{225°, 90°, 144.74°+6.0°\}$
Orientation [111]B	[0.53, 0.53, 0.66]	[0.47, 0.47, -0.75]	[$\bar{1}$10]	$\{225°, 90°, 144.74°-6.0°\}$
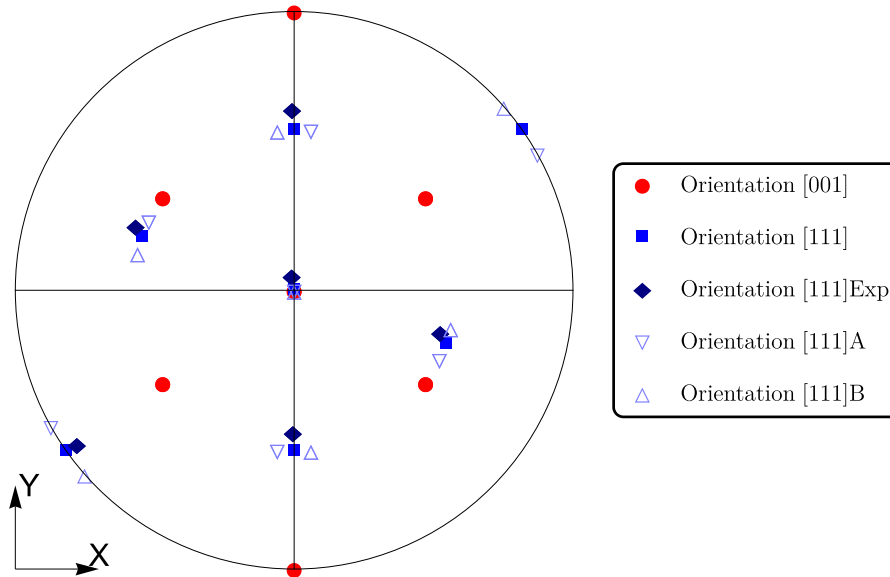
Fig. 2. Pole figure {011} showing the orientations listed in Table 2.

the ideal [111] orientation by 6° clockwise and counterclockwise around the z-axis, respectively, so that the sample plane remains a symmetry plane of the crystal. All five orientations are also displayed in the pole figure {011} in Fig. 2.

To replicate the boundary and loading conditions of the experiment, the following conditions are imposed in all FE calculations:

$$\mathbf{u}(0, y, z) = \mathbf{0} \quad \text{and} \quad \mathbf{u}(x_{\max}, y, z) = \dot{\delta}t\mathbf{i}_x \tag{15}$$

where $\dot{\delta}$ is a constant displacement rate equal to 0.01 mm/s.

3.3. Finite element implementation

The standard procedures developed for the finite element implementation of finite deformation rate-dependent elasto-plasticity in a fully Lagrangian, displacement-based setting by Simo and Hughes (1998) are employed. Incremental constitutive equations are obtained using an implicit backward-Euler time integration scheme, and Eq. (2) is integrated using the exponential map:

$$\mathbf{F}_p(t + \Delta t) = \exp(\Delta t\hat{\mathbf{L}}_p)\mathbf{F}_p(t). \tag{16}$$

The FE implementation is carried out using the AceGen/AceFEM packages (Korelc, 2002), following similar implementations for FCC crystals with slip-only mechanisms (Kucharski et al., 2014; Frydrych and Kowalczyk-Gajewska, 2018). The AceGen package facilitates the derivation of an algorithmic consistent tangent, enabling quadratic convergence. The tool combines the symbolic algebra capabilities of Wolfram Mathematica with automatic differentiation and advanced expression optimization techniques. Computations are performed using the associated AceFEM package. The finite elements used are 20-noded hexahedral elements with reduced integration. Regarding the reorientation condition, it is checked at each Gauss point after global convergence is reached. This treatment is, to some extent, similar to that applied by Zhang and Joshi (2012) and Liu and Wei (2014).

Several techniques recently proposed in the literature have been incorporated to further enhance the computational efficiency of the framework, namely:

Table 3
Elastic constants (Clausen et al., 1998) and other pre-set parameters for single-crystal Hadfield steel.

C_{11} [GPa]	C_{12} [GPa]	C_{44} [GPa]	γ^{TW}	n	$\dot{\gamma}_0$
204.6	137.7	126.2	$1/\sqrt{2}$	20	0.001

Table 4
Constitutive parameters identified based on tensile test results of dog-bone specimens.

System	Interaction	τ_0^c [MPa]	h_0 [MPa]	h_1 [MPa]	τ_{sat}/f_{sat} [MPa]/–	q
Virgin crystal (slip and twinning active)						
Slip	Slip–slip	126.5	6.07	379.5	48.0	1.0
	Slip–twin	–	–	–	–	–
Twin	Twin–slip	–	0	210.0	–	1.0
	Twin–twin	112.9	26.25	–	0.99	1.0
Crystal after reorientation (only slip active)						
Slip	Slip–slip	139.1	154.5	49.36	−39.48	1.0

- Reduction of the number of internal variables for which residual equations are solved at the Gauss point level from 24 to 11, following (Dittmann and Wulfinghoff, 2023). In this approach, 9 components of Mandel stress, accumulated slip, and accumulated twin are used instead of 24 accumulated shears in 24 slip and twin modes (possible when latent hardening coefficients for system interactions are set to 1).
- Use of the line-search method (Mànik et al., 2022) to track the solution path, which accelerates convergence in the presence of reorientation events.
- Use of the exact matrix exponent formula Korelc and Stupkiewicz (2014) in the exponential map step specified by Eq. (16).

3.4. Identification of the constitutive parameters

The elastic constants describing the anisotropic elasticity of a single crystal with cubic symmetry for Hadfield steel are assumed as given in Table 3, following Clausen et al. (1998). Since quasi-static processes are analyzed and strain rate effects are not investigated in the present study, the rate sensitivity parameters of the model, n and $\dot{\gamma}_0$, are pre-set to 20 and 0.001 [1/s], respectively. With these assumptions and the preliminary simplifications regarding interactions between deformation modes discussed in Section 3.1, twelve constitutive parameters remain to be identified.

These parameters are determined based on uniaxial tensile test results of specimens without notches, for two single-crystal orientations. For the ⟨001⟩ orientation, where only slip was experimentally observed, the test results are used to calibrate parameters governing slip–slip interactions in the virgin crystal. For the ⟨111⟩ orientation, where twinning was the dominant mechanism, the test results are used to identify parameters describing twin–twin and twin–slip interactions in the virgin crystal, as well as those relevant for the reoriented material that deforms by slip alone.

An initial range of possible parameter values was established, and then optimized using a genetic algorithm, following the methodology described in Frydrych et al. (2020). The final set of identified parameters is listed in Table 4. All calculations in this paper are performed using the same set of material parameters.

A few previous studies have attempted to identify CP parameters for single crystals of Hadfield steel. Karaman et al. (2000a) performed identification based on tensile test results for the ⟨111⟩ orientation only. Although some similarities exist between their formulation and the present one, the crystal plasticity model – particularly in its hardening description – differs from the current approach, making direct comparison of all parameters not possible. In their study, the initial critical shear stress for slip was slightly smaller than for twinning (110 MPa vs. 115 MPa). A similar qualitative relation between these parameters was also applied in Kowalczyk-Gajewska (2010) in the context of the VPSC implementation of the PTVC scheme. In the present study, using experimental curves for two orientations, it was found that both quantities are still close to each other, with the initial τ_c for twinning smaller than for slip. Quantitatively, these values are of comparable magnitude. In Lindroos et al. (2018), the initial τ_c was identified as almost equal for slip and twinning mechanisms (87 MPa and 90 MPa, respectively). Material parameters in that work were identified based on the response of two orientations, ⟨001⟩ and ⟨111⟩, in tension and compression; however, instead of a full 3D sample model, an RVE with isovolumetric grains and fixed boundary conditions on the RVE sides was used for the identification procedure.

4. Results and discussion

4.1. Deformation under uniaxial tension

The normalized force–displacement response of dog-bone specimens with crystal orientations [001] and [111] subjected to uniaxial tension, as obtained from experiments and predicted using CPFE simulations, is shown in Fig. 3(a). The normalized force is defined
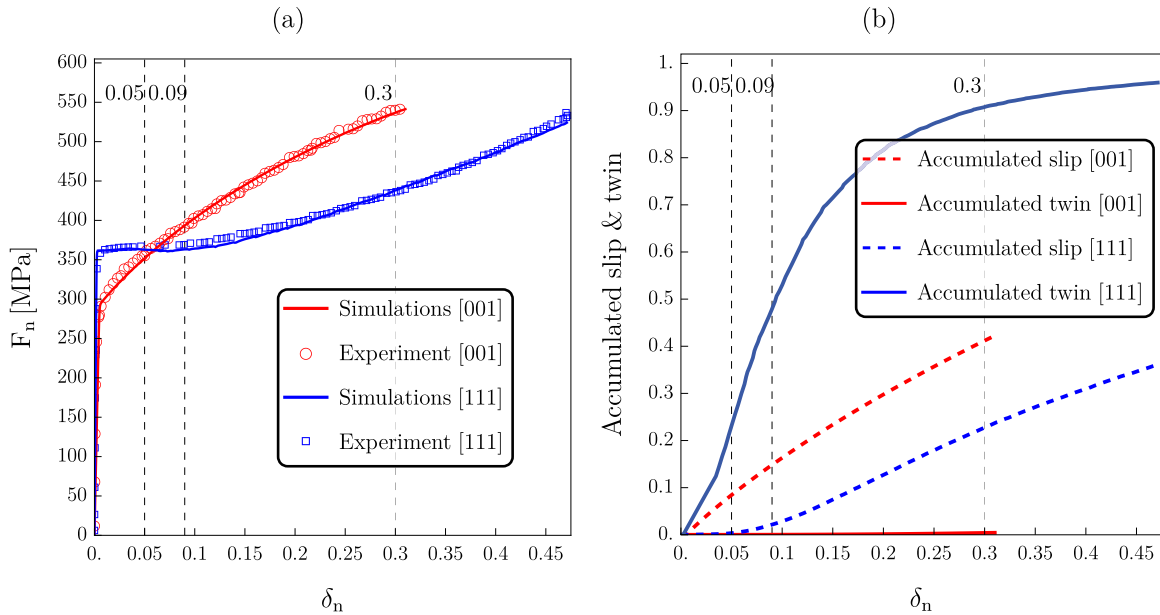
Fig. 3. (a) Comparison of experimentally obtained and predicted normalized force–displacement ($F_n - \delta_n$) curves for dog-bone specimens with crystal orientations [001] and [111] subjected to uniaxial tension. (b) Predicted evolution of accumulated slip and twin volume fractions, averaged over the gauge region of the specimen for the two orientations.

as $F_n = F/A_0$ and the normalized displacement as $\delta_n = \dot{\delta}t/L_0$, where F is the total reaction force, A_0 is the initial cross-sectional area of the specimen gauge section, and L_0 is the initial gauge length. Although the experimental results in Fig. 3(a) were used for the identification of constitutive parameters in Section 3.4, the near-perfect agreement between experiments and simulations for both [001]- and [111]-oriented dog-bone specimens not only demonstrates the quality of the parameter identification, but also confirms that the constitutive model described in Section 3.1 can accurately capture slip and twinning deformation mechanisms in austenitic manganese steel.

The predicted evolution of accumulated slip and twin volume fraction in the gauge section of the dog-bone specimens is shown in Fig. 3(b). These two quantities are defined as:

$$\bar{\Gamma} = \frac{\sum_i \Gamma_i V_i}{\sum_i V_i} \quad \bar{f}^{TW} = \frac{\sum_i f_i^{TW} V_i}{\sum_i V_i} \tag{17}$$

where Γ_i is the accumulated slip, f_i^{TW} is the twin volume fraction, and V_i is the volume associated with the ith Gauss point. Note that if reorientation has occurred at a given Gauss point, the twin volume fraction at that point is set to one.

The results in Fig. 3(a) clearly show that the fully calibrated CPFE simulations accurately predict the experimentally observed strain-hardening response for both [001]- and [111]-oriented specimens. Specifically, the model captures the initially high but continuously decreasing hardening rate (i.e., concave downward stress–strain curve) for the [001] specimen, and the initial near-zero hardening followed by a concave upward stress–strain curve for the [111] specimen. These orientation-dependent hardening behaviors reflect the underlying deformation mechanisms in the material.

As shown in Fig. 3(b), twinning activity is negligible for the [001] orientation, with deformation governed primarily by slip accumulation. In contrast, significant twinning is observed for the [111] orientation. For this case, the twin volume fraction reaches approximately 0.5 at a nominal strain of 0.09. Beyond this point, the rate of increase in twin volume fraction slows and eventually saturates at a value of about 0.95. At the same time, slip remains nearly inactive up to a nominal strain of 0.1. After this point, a steady increase in accumulated slip is observed as slip becomes active within the reoriented regions of the specimen. The initial low-hardening stage in the [111] stress–strain curve corresponds to twinning-dominated deformation. Once twinning saturates and slip becomes the dominant mechanism, the hardening rate begins to rise—marking the transition from initial near-zero hardening to concave upward stress–strain response for the [111] orientation.

The distribution of accumulated slip and twin volume fraction in the gauge section of dog-bone specimens with crystal orientations [001] and [111] at three levels of imposed displacement is shown in Fig. 4. In the [001] specimen, deformation is dominated by slip, which remains fairly uniform throughout the gauge section. However, some twinning activity is observed in the fillet region near the gauge section at larger imposed displacements. In contrast, during the early stages of deformation in the [111] specimens, the gauge section is dominated by twinning, with almost no slip activity observed. At larger imposed displacements, when twinning tends to saturate, i.e., most regions in the gauge section have already twinned and reoriented, slip activity in the reoriented regions begins to dominate the deformation. Notably, due to the probabilistic, twin-volume-consistent reorientation
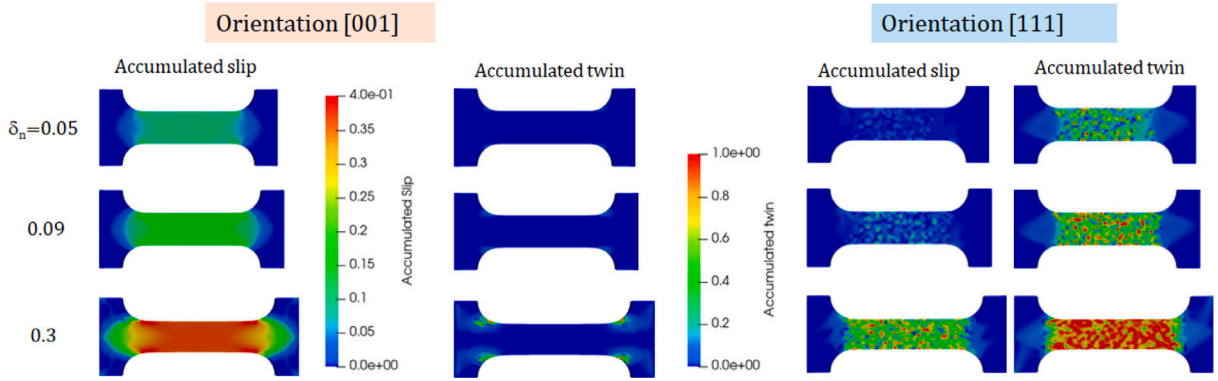
Fig. 4. Contour plots showing the predicted evolution of accumulated slip and twin volume fraction in dog-bone specimens with crystal orientations [001] and [111] subjected to uniaxial tension. Results are shown at three levels of normalized displacement: $\delta_n = 0.05$, 0.09, and 0.3, which are also marked in Fig. 3.

scheme employed in this work, twinning in the gauge section occurs in discrete regions. Because the crystal plasticity formulation used here is local, it does not produce continuous twin bands spanning the width of the gauge section, as seen in the single-crystal experiments by Zheng et al. (2025). Nevertheless, our results are in perfect agreement with EBSD observations. reported in Zheng et al. (2025), which show extensive twinning activity when the material is under tension in the [111] direction and hardly any such activity for tension in the [001] direction.

It has also been confirmed that, in agreement with the highest Schmid factors, three twin systems – $(111)[11\bar{2}]$, $(\bar{1}11)[\bar{1}\bar{2}1]$, and $(1\bar{1}1)[\bar{2}\bar{1}1]$ – are active when the tension axis is perfectly aligned with the crystallographic direction $[11\bar{1}]$, while a single twin system, $(1\bar{1}1)[\bar{2}\bar{1}1]$, is predominantly active when the tension axis is slightly misoriented with respect to the $[11\bar{1}]$ direction, as in the case of orientation [111]Exp. According to the reorientation scheme used in this work, the new orientation, assumed once the reorientation condition is met, corresponds to the most active twin system at the given point. For the [111] case, this results in the appearance of areas with one new twin-related orientation. This finding is in agreement with the EBSD observations of Zheng et al. (2025). Moreover, when observing the area fraction of twins shown in Fig. 2b of Zheng et al. (2025) in conjunction with the DIC maps in Fig. 3 therein, the layers of intensive strain can be correlated with the twinned regions. Using these experimental findings, it is also possible to verify that the evolution of twin volume fraction with strain shown in Fig. 3b is correctly captured by the present approach.

### 4.2. Influence of notch on deformation

We now analyze the effect of a notch on the orientation-dependent deformation response and mechanisms of single-crystal austenitic manganese steel. In particular, we analyze single-edge notch specimens with the loading axis aligned along either the [001] or [111] crystallographic directions. In the simulations, for the [111] orientation, parametric studies are also conducted to assess the effect of small deviations from the exact orientation. All orientation cases analyzed are listed in Table 2.

Fig. 5(a) shows the predicted normalized force–displacement (F_n–δ_n) curves for single-edge notch specimens, while the experimentally obtained results are shown in Fig. 5(b). As with the dog-bone specimens, $\delta_n = \dot{\delta}t/L_0$, where L_0 is the gauge length, and $F_n = F/A_0$, where F is the total reaction force. However, for single-edge notch specimens, A_0 is the cross-sectional area of the ligament, i.e., the cross-sectional area of the gauge section minus the cross-sectional area removed by the notch. Note that, unlike the dog-bone specimens where extensometers were used in the experiments, the force–displacement curves for single-edge notch specimens are not corrected for machine compliance. Nevertheless, the predicted and experimental results show very good qualitative agreement. For example, both simulation and experiment show greater strain hardening in the [001] specimens than in the [111] specimens, and neither shows a concave-upward hardening response for the notched [111] specimens. Additionally, a comparison of the F_n–δ_n curves for dog-bone specimens in Fig. 3(a) and for single-edge notch specimens in Fig. 5 clearly demonstrates a notch-strengthening effect in both [001] and [111] specimens, in both experimental and simulation results. Furthermore, simulation results from the parametric studies show that small deviations from the exact [111] orientation do not significantly affect the F_n–δ_n response of single-edge notch specimens, apart from slight differences in the early stages of deformation.

The predicted evolution of accumulated slip and twin volume fraction, averaged over the entire gauge region of the single-edge notch specimens, is shown in Fig. 6(a) and (b), respectively. As in the dog-bone specimens (Fig. 3(b)), deformation in the [001] specimen is primarily governed by slip, while twinning dominates in all four [111] variants. However, due to the presence of the notch, which results in a more complex stress state, a modest amount of twinning activity is also observed in the [001] single-edge notch specimen. This was almost entirely absent in the [001]-oriented dog-bone specimen. Furthermore, in the [111] single-edge notch specimens, slip activity is observed even at early stages of deformation. In contrast, in the dog-bone specimens, slip becomes active only after significant twinning and reorientation. For example, at $\delta_n = 0.05$, there is already a small but noticeable amount
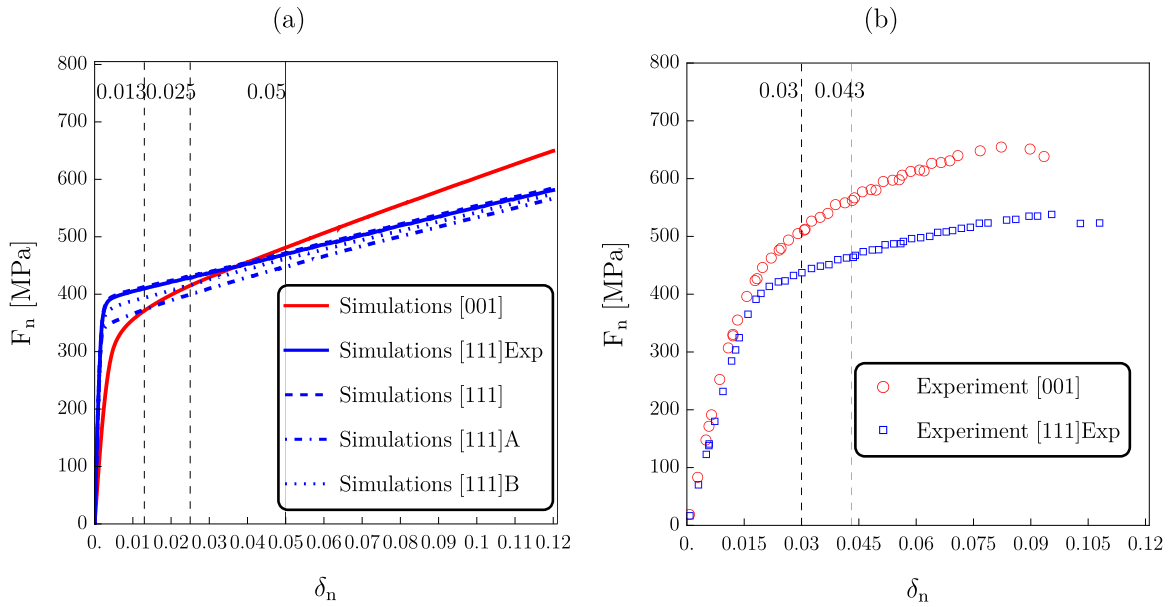
Fig. 5. (a) Predicted normalized force–displacement (F_n–δ_n) curves for single-edge notch specimens with crystal orientations [001] and [111]. For the [111] orientation, parametric studies are also conducted to assess the effect of deviations from the exact [111] orientation. All orientation cases analyzed are listed in Table 2. (b) Experimentally obtained F_n–δ_n curves for single-edge notch specimens with crystal orientations [001] and [111]Exp.
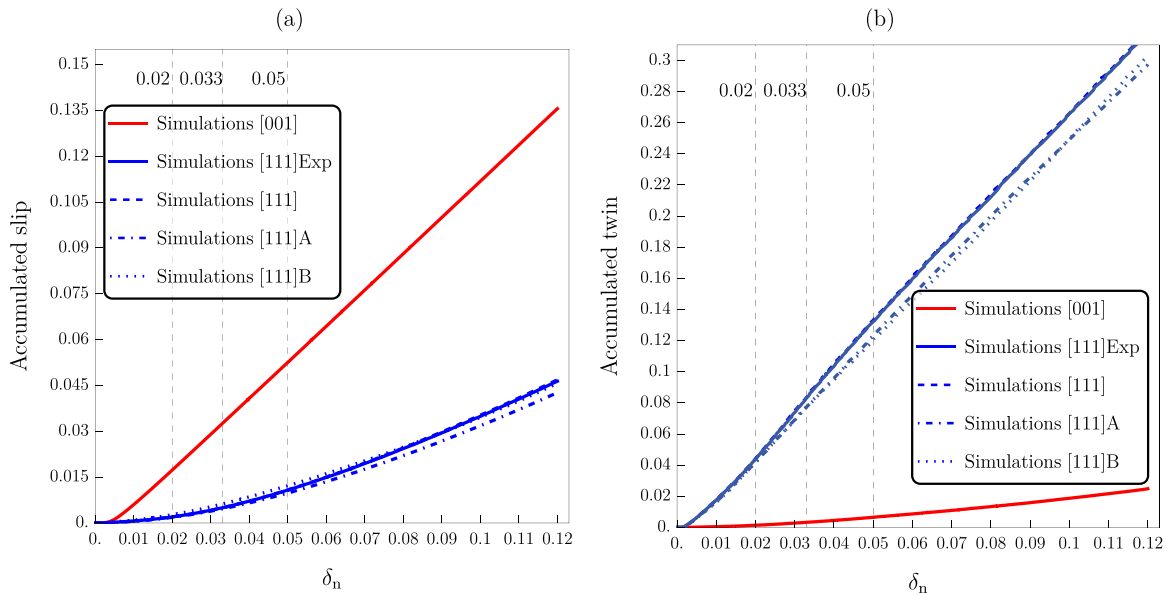
Fig. 6. Predicted evolution of (a) accumulated slip and (b) twin volume fraction, averaged over the gauge region of single-edge notch specimens with crystal orientations [001] and [111]. For the [111] orientation, parametric studies are conducted to assess the effect of deviations from the exact [111] orientation. All orientation cases analyzed are listed in Table 2.

of accumulated slip in the [111]-oriented single-edge notch specimen (Fig. 6(a)). At the same δ_n, the accumulated slip in the [111]-oriented dog-bone specimen is essentially zero (Fig. 3(b)). This increase in slip is consistent with the differences in strain-hardening behavior between the [111]-oriented dog-bone specimens (Fig. 3(a)) and the single-edge notch specimens (Fig. 5(a)), particularly the absence of the early-stage non-hardening regime in the [111] single-edge notch response.

Contour plots of accumulated slip and twin volume fraction for the [001] and [111]Exp specimens at $\delta_n = 0.05$ are shown in Fig. 7. In both cases, slip and twinning activity are concentrated near the notch tip. Although deformation is confined to this region,
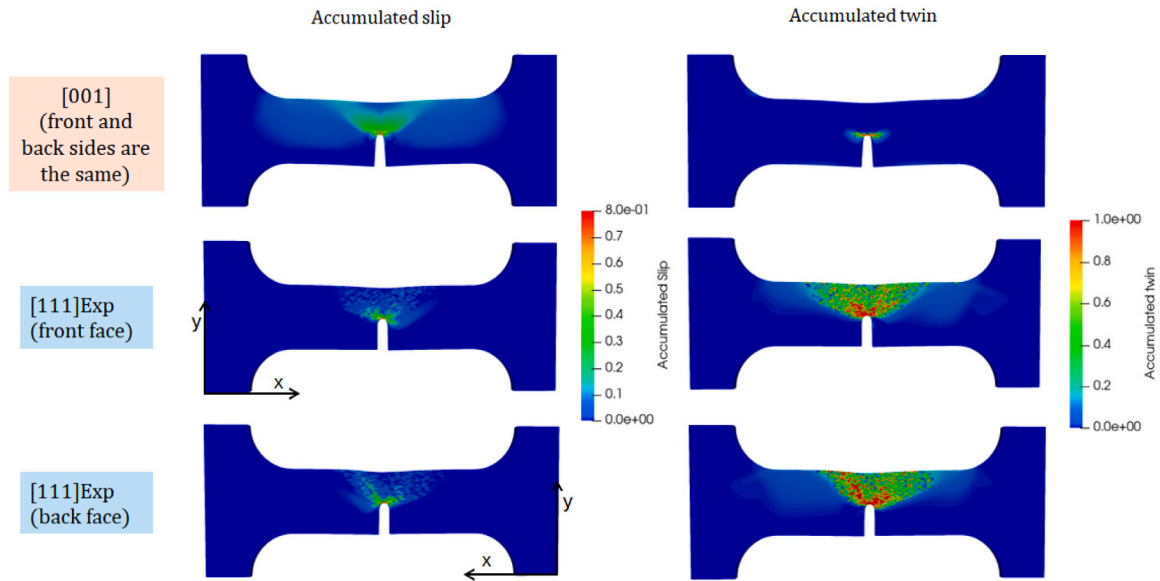
Fig. 7. Contour plots showing the predicted evolution of accumulated slip and twin volume fraction in single-edge notch specimens with crystal orientations [001] and [111]Exp (see Table 2) at a normalized displacement $\delta_n = 0.05$, which is also indicated in Figs. 5 and 6.

twinning occurs in discrete pockets. The twin volume fraction in these pockets rapidly evolves to one. Once reoriented, these regions continue to deform by slip. This behavior explains the early onset of slip activity in the [111]-oriented single-edge notch specimens.

For the [001]-oriented specimen, the distributions of both slip and twin volume fraction are symmetric with respect to the notch. In contrast, for the [111]Exp-oriented specimen, both slip and twinning are clearly asymmetric across the notch. This in-plane asymmetry in twinning activity for the [111] orientation is consistent with the experimental observations reported by Zheng et al. (2025). As seen in Fig. 7, there is also an out-of-plane asymmetry in the deformation pattern between the front and back faces of the [111]Exp specimen. This asymmetry arises from the inclination of the sample plane with respect to the {011} crystal plane, which is a symmetry plane of the FCC lattice. This front–back asymmetry is not observed in the other three [111] specimens analyzed computationally, where the sample plane remains aligned with {011}. However, small differences between the two faces may still occur due to the probabilistic nature of the reorientation scheme.

4.3. Slip–twinning–notch interaction and failure implications

We now focus on understanding the interaction between the two deformation mechanisms, slip and twinning, and the effect of a notch on the orientation-dependent mechanical response of single-crystal austenitic manganese steel. To this end, we carry out simulations in which the twinning mechanism is selectively activated in both [001]- and [111]-oriented dog-bone as well as [001]- and [111]Exp-oriented single-edge notch specimens. All calculations are performed using the same set of parameters listed in Section 3.4, and the full description of the crystallographic orientations of the specimens is given in Table 2. For the cases without twinning, the contributions from twinning are simply disabled.

Fig. 8 presents the normalized force (F_n) versus normalized displacement (δ_n) response of [001]- and [111]-oriented dog-bone as well as [001]- and [111]Exp-single-edge notch specimens, with and without deformation twinning included in the simulations. As seen in Fig. 8, the mechanical response of both [001]-oriented dog-bone and single-edge notch specimens is largely insensitive to whether twinning is active. A comparison of Fig. 8(a) and (b) also shows that the presence of a notch in the [001]-oriented specimen leads to a strengthening effect. This is evident from both the increase in the value of F_n at the onset of nonlinearity in the F_n–δ_n response and the higher F_n values observed during subsequent loading. This notch-strengthening effect is present at least prior to fracture, even in the experimental results, as shown in Sections 4.1 and 4.2.

In contrast, as seen in Fig. 8, activation of twinning has a pronounced effect on the F_n–δ_n response of both [111]-oriented dog-bone and [111]Exp-oriented single-edge notch specimens. In both cases, when twinning is disabled, the value of F_n at the onset of nonlinearity is significantly higher, and higher F_n values are observed throughout subsequent loading. Importantly, in the absence of twinning, the initially non-hardening (nearly flat F_n–δ_n) response is entirely absent in the [111]Exp-oriented dog-bone specimen. Additionally, without twinning, the [111]-oriented dog-bone and [111]Exp-oriented single-edge notch specimens exhibit the onset of nonlinearity at an F_n value approximately 1.5 times greater than that of the corresponding [001]-oriented specimens. This behavior is consistent with the relative Schmid factors associated with these orientations. However, when twinning is active, the difference in the F_n value at the onset of nonlinearity between the [111]- and [001]-oriented specimens is relatively small.
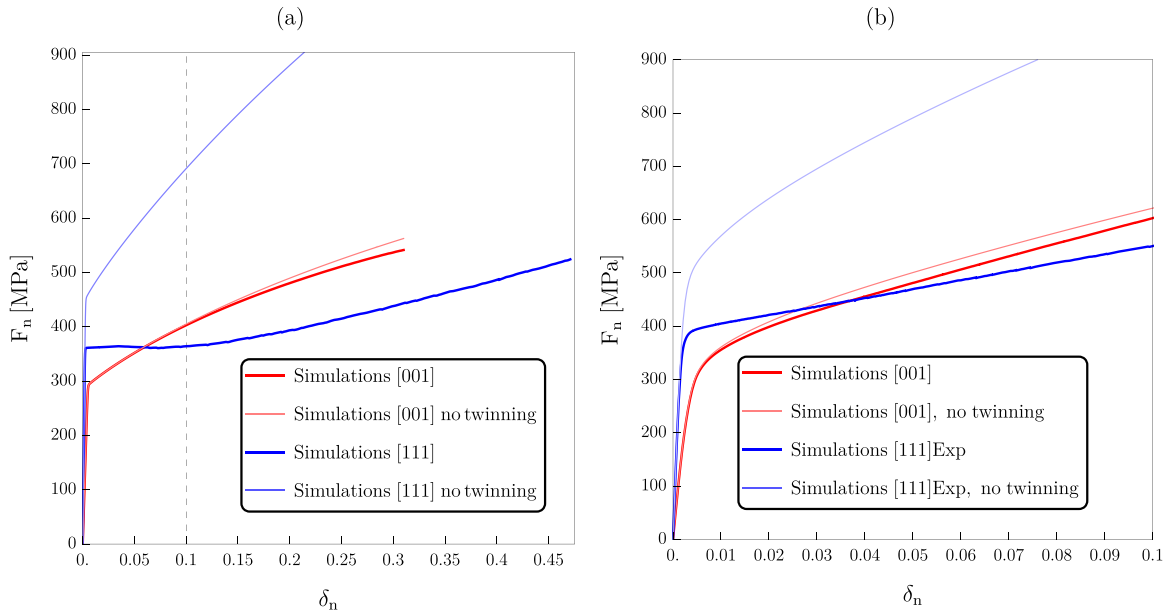
Fig. 8. Predicted normalized force–displacement (F_n–δ_n) curves for (a) dog-bone specimens with crystal orientations [001] and [111] and (b) single-edge notch specimens with crystal orientations [001] and [111]Exp (see Table 2), with and without deformation twinning.

The distribution of accumulated slip and twin volume fraction in the [001]- and [111]Exp-oriented single-edge notch specimens at the same three imposed displacements is shown in Figs. 9 and 10, respectively. In both figures, results are also shown for scenarios where twinning is assumed to be absent. In both the [001]- and [111]Exp-oriented single-edge notch specimens, deformation is concentrated near the notch. In the [001]-oriented specimen, deformation is symmetric across the notch and is largely governed by accumulated slip. A narrow and relatively small zone surrounding the notch in the [001]-oriented specimen does exhibit twinning, which arises due to the multiaxial stress state that develops near the notch tip. However, the overall distribution of accumulated slip in the [001]-oriented single-edge notch specimen is similar with and without twinning. The only difference is that, since twinning in the simulations occurs in discrete regions, it introduces some additional spatial discreteness in the slip distribution near the notch tip.

In the [111]Exp-oriented single-edge notch specimen (Fig. 10), deformation is largely governed by twinning, and the distribution of both accumulated slip and twin volume fraction is asymmetric across the notch. The accumulated slip is concentrated in three distinct regions. Two of these correspond to areas where twinning is also dominant. However, one region – located behind the notch tip and below the notch (on the right side of the notch in Fig. 10) – exhibits significant slip activity without any observed twinning. This slip-dominated region contributes to the flattening of the initially circular notch tip. While the distribution of accumulated slip remains asymmetric even in the absence of twinning, the additional spatial discreteness associated with twinning reorientation is absent, and the deformation of the notch tip is comparatively less pronounced. Although not shown here, the other [111] orientations (see Table 2) also qualitatively show similar distributions of accumulated slip and twinning near the deforming notch.

The asymmetric deformation field in the [111]Exp-oriented notched specimen, as shown in Fig. 10, leads to asymmetric notch deformation. This notch asymmetry is further analyzed in Fig. 11. The plots in Fig. 11(b) and (c) show the differences in the displacement components u_y and u_z, respectively, between two nodes A and B located on either side of the notch, as schematically illustrated in Fig. 11(a). These displacement differences are normalized by the initial notch width, $w = 90\,\mu$m. In the case of a perfectly symmetric notch opening, the normalized values would be zero.

The in-plane asymmetry of the notch opening, quantified by $\Delta u_y/w$ in Fig. 11(b), varies among the different orientations. It is negligible for the [001]-oriented specimen and is strongly influenced by the misorientation of the [111] direction with respect to the specimen axis in the four other [111] cases. The largest asymmetry is observed for the [111]A specimen, in which the [111] direction is rotated by 6° clockwise about the z-axis. A similar level of asymmetry is also observed when twinning is disabled, indicating that this effect primarily arises from crystallographic anisotropy.

As previously discussed in relation to Fig. 7, the asymmetry in the z-direction, shown in Fig. 11(c), is much smaller than the asymmetry in the y-direction. The z-direction asymmetry is observed primarily for the [111]Exp orientation, in which the sample plane is misaligned with respect to the ($\bar{1}$10) crystallographic plane. Even in this case, however, the ratio $\Delta u_z/w$ is at least an order of magnitude smaller than $\Delta u_y/w$. For the other orientations, fluctuations in $\Delta u_z/w$ are nearly two orders of magnitude smaller and are attributed to the probabilistic nature of the twin reorientation scheme. As expected, when twinning is disabled, the value of $\Delta u_z/w$ is exactly zero.

In Fig. 12, we compare the deformed shape of the notch in both [001]- and [111]Exp-oriented single-edge notch specimens as observed in experiments and as predicted by simulations. The results are also shown for the [111]Exp-oriented specimen under
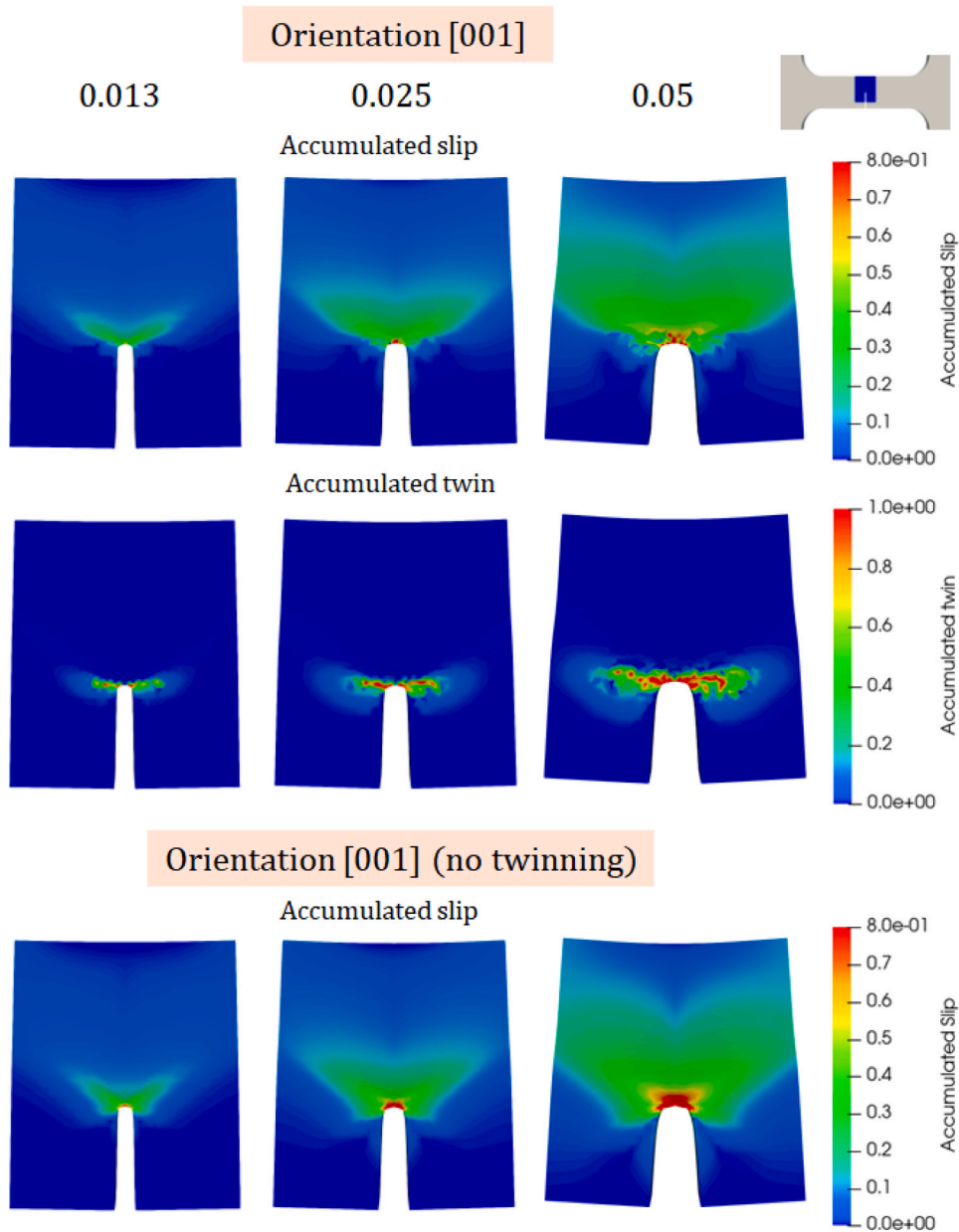
Fig. 9. Contour plots showing the predicted evolution of accumulated slip and twin volume fraction in [001]-oriented single-edge notch specimen at three normalized displacements $\delta_n = 0.013, 0.025$, and 0.05. Also shown are the contour plots of accumulated slip in [001]-oriented single-edge notch specimen at the same three normalized displacements for a scenario where twinning is assumed to be absent.

a scenario where twinning is assumed to be absent. For a meaningful comparison, all results are presented at approximately the same current notch width, since the experimentally measured normalized displacement (δ_n) of the entire specimen is not directly comparable to simulation values due to machine compliance effects in the experimental setup. The values of δ_n indicated in the figure for both the experiments and the simulations correspond to those marked in Figs. 5(a) and (b), respectively.

As seen in the figure, there is very good agreement between the experimentally observed and simulated notch shapes. For the [001]-oriented specimen, consistent with experimental observations, the simulations predict that the initially semi-circular notch tip flattens and opens symmetrically. For the [111]Exp-oriented specimen, the notch tip also flattens, but the flattened edge is inclined toward one side, resulting in a highly asymmetric overall notch deformation. Predictions for the [111]Exp-oriented specimen without twinning show that the deformation of the notch remains asymmetric, although the extent of asymmetry and notch tip flattening is significantly reduced compared to the case with active twinning.
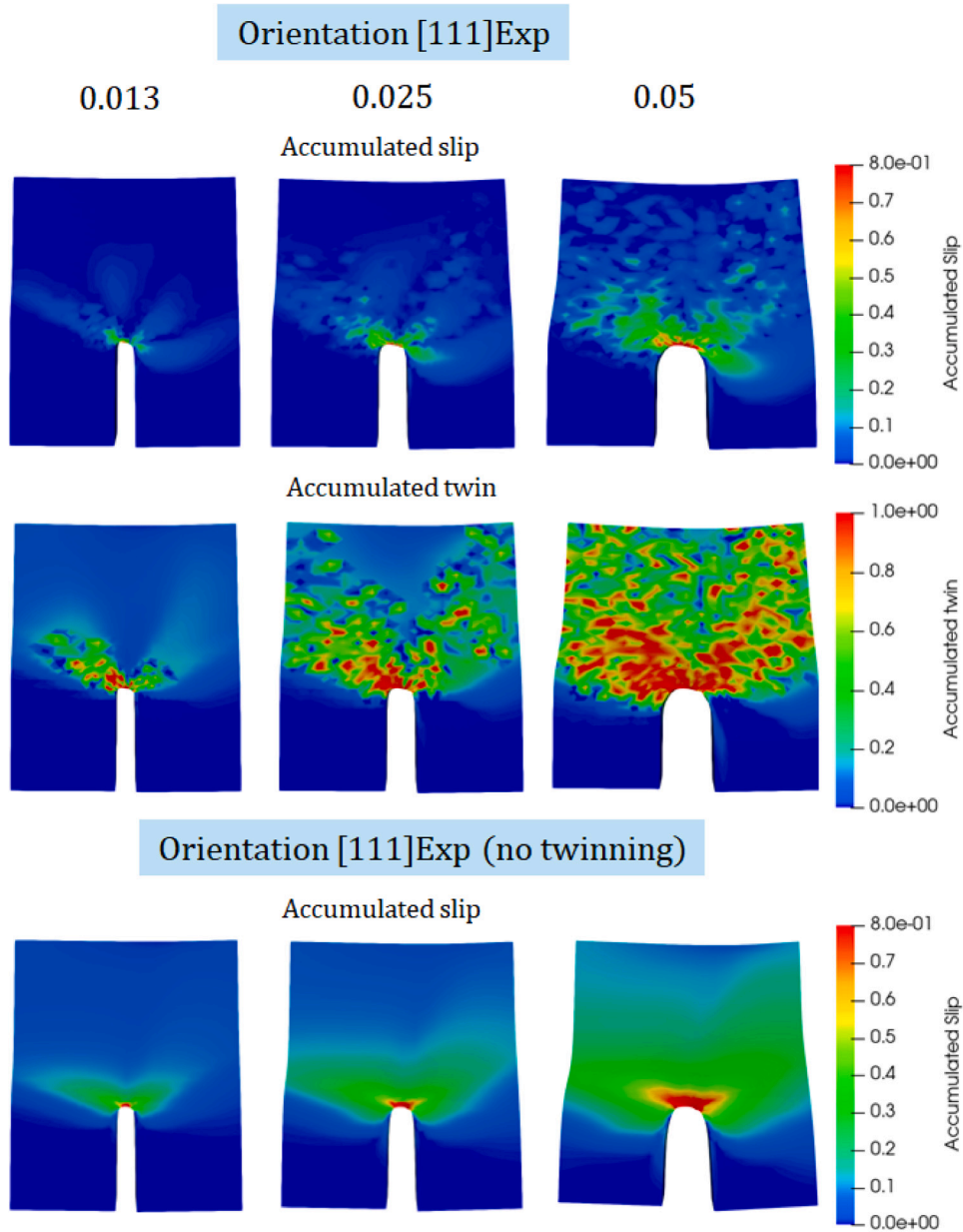
Fig. 10. Contour plots showing the predicted evolution of accumulated slip and twin volume fraction in [111]Exp-oriented single-edge notch specimen at three normalized displacements $\delta_n = 0.013, 0.025$, and 0.05. Also shown are the contour plots of accumulated slip in [111]Exp-oriented single-edge notch specimen at the same three normalized displacements for a scenario where twinning is assumed to be absent.

The asymmetric deformation of an initially symmetric discontinuity in FCC crystals has also been observed in other contexts. For example, in the work by Srivastava and Needleman (2015), which focused on the effect of crystal orientation on the evolution of initially spherical voids in FCC single crystals subjected to tensile creep loading, it was found that when the maximum principal stress direction was aligned with the $\langle 111 \rangle$ crystallographic direction, both the matrix and the initially spherical void deformed asymmetrically, even under high imposed stress triaxiality (defined as the ratio of the first to the second stress invariants). The void evolved into a polygonal shape with rounded corners, highlighting the inherent anisotropy-driven asymmetry in crystal plasticity.

In the experiments of Zheng et al. (2025), it was observed that for [001]-oriented single-edge notch specimens, a single crack nucleated from the center of the symmetrically deforming notch, whereas for [111]Exp-oriented specimens, multiple microcracks nucleated along the periphery of the asymmetrically deforming notch. Although crack nucleation is not explicitly modeled in this work, Fig. 13 presents the predicted distribution of maximum principal stress ($\Sigma_{\max}$), mean stress (Σ_m), and stress triaxiality (T)
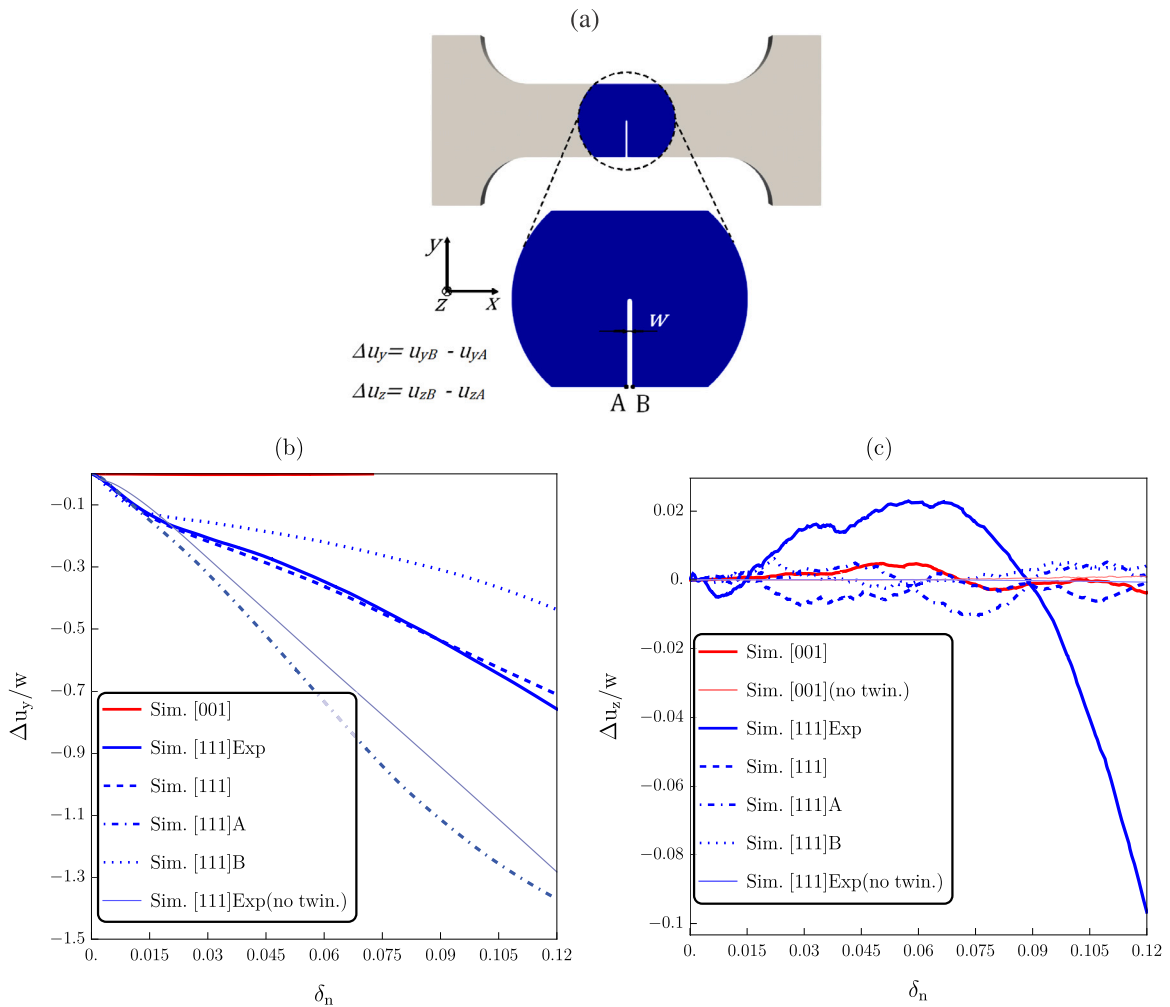
Fig. 11. (a) Schematic illustrating two parameters, Δu_y and Δu_z, used to characterize asymmetric notch opening in single-edge notch specimens. Evolution of predicted (b) normalized Δu_y and (c) normalized Δu_z with normalized displacement δ_n for various orientations of the single-edge notch specimens. All orientation cases analyzed are listed in Table 2. Results are also shown for the [111]Exp-oriented specimen under the assumption that twinning is absent.

in both [001]- and [111]Exp-oriented single-edge notch specimens under scenarios where deformation twinning is either active or suppressed. These parameters provide insight into the propensity for crack initiation.

As shown in the figure, for the [001]-oriented specimen, with or without twinning, the distributions of Σ_{max}, Σ_m, and T are nearly symmetric across the notch, and their peak values – particularly those of T – are concentrated along the centerline of the symmetrically deforming notch. This suggests a tendency for the nucleation of a single ductile crack from the notch center. In contrast, for the [111]Exp-oriented specimen, again with or without twinning, the distributions of Σ_{max}, Σ_m, and T are clearly asymmetric across the notch. Their maxima, in the case with twinning, are not concentrated in a single region along the centerline, as observed in the [001] case. Of particular importance is the distribution of T around the deformed notch in the [111] Exp specimen, which shows elevated values in discrete pockets, including along the periphery of the asymmetrically deformed notch. This spatial pattern suggests a greater propensity for the nucleation of multiple ductile cracks along the notch periphery in the [111] Exp-oriented case.

5. Summary and concluding remarks

This work is motivated by the recent in-situ experimental observations by Zheng et al. (2025), in which the deformation and fracture behavior of an austenitic manganese steel was examined using ⟨001⟩- and ⟨111⟩-oriented single-crystal dog-bone and single-edge notch tension specimens. To explain these observations and deconvolute the interaction of slip, twinning, and notch, we carried out detailed finite element simulations using a rate-dependent crystal plasticity framework that incorporates both crystallographic
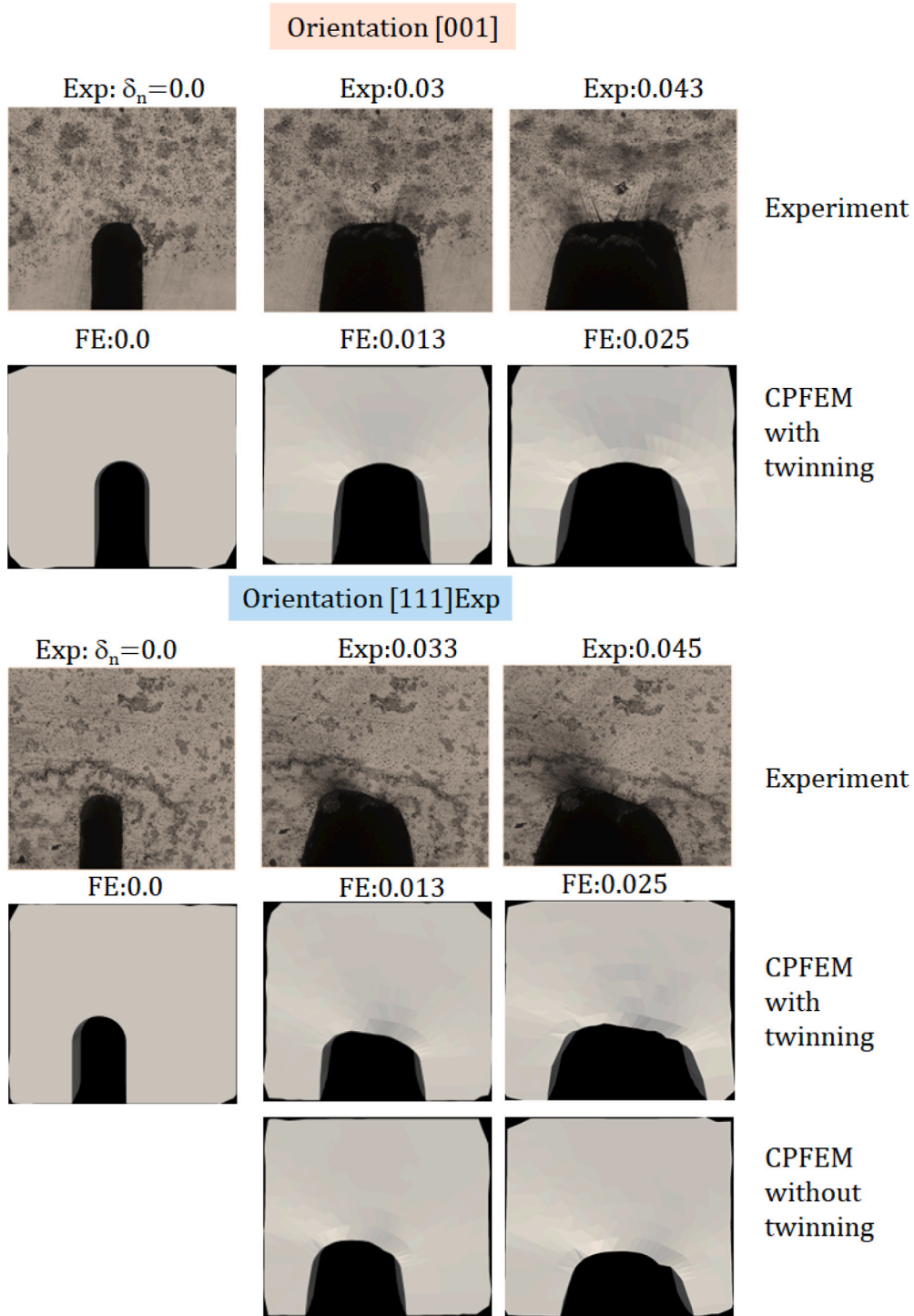
Fig. 12. Comparison of experimentally observed and predicted notch root shapes in [001] and [111]Exp-oriented single-edge notch specimens (see Table 2) at two values of the imposed normalized displacement (δ_n). For the [111]Exp-oriented specimen, predictions are also shown for a scenario where twinning is assumed to be absent. The region shown in both experimental images and predictions spans approximately 330 μm (height) × 375 μm (width).

slip and deformation twinning. Limited experiments on single-crystal dog-bone and single-edge notch specimens, with loading axes aligned close to $\langle 001 \rangle$ or $\langle 111 \rangle$, were also conducted to aid the simulations. Several features of the experimental observations are
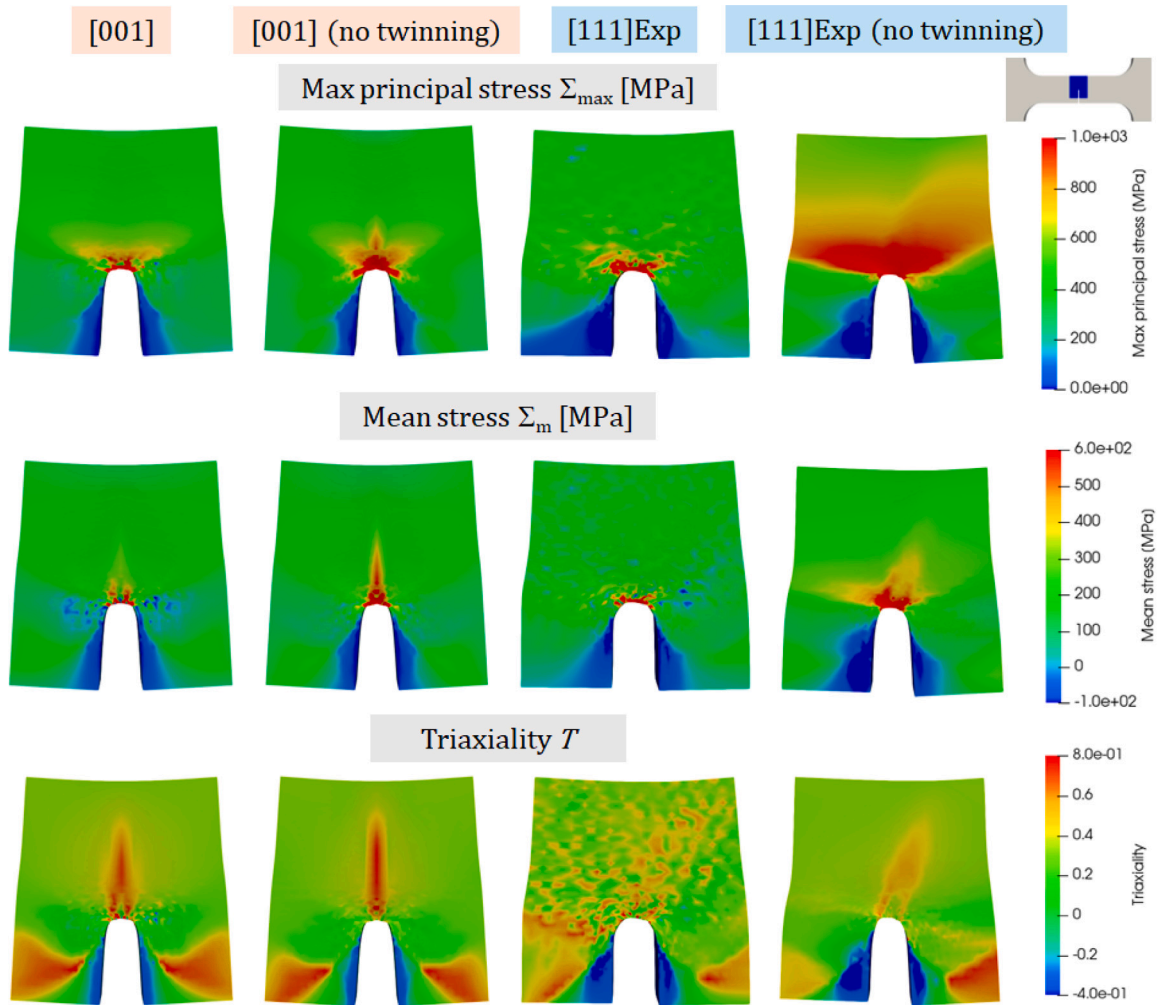
Fig. 13. Contour plots showing the predicted distribution of maximum principal stress (Σ_{max}), mean stress (Σ_m), and triaxiality (T) at a normalized displacement $\delta_n = 0.05$ in single-edge notch specimens with crystal orientations [001] and [111]Exp (see Table 2), with and without deformation twinning.

accurately captured in the simulations, and the underlying mechanisms are clarified. The key findings of this study are summarized below:

- The fully calibrated crystal plasticity finite element (CPFE) simulations accurately reproduce the distinct stress–strain responses observed experimentally for ⟨001⟩- and ⟨111⟩-oriented dog-bone specimens. In particular, the simulations quantitatively capture the initially high strain-hardening followed by a concave downward response in the ⟨001⟩ specimens, and the initial near-zero strain-hardening followed by a concave upward response in the ⟨111⟩ specimens.
- Consistent with experiments, the simulations show negligible twinning activity in ⟨001⟩-oriented dog-bone specimens and twinning-dominated deformation in the ⟨111⟩-oriented ones. The accumulated slip increases monotonically in the ⟨001⟩ specimens, while in the ⟨111⟩ specimens, slip becomes active only after twinning saturates. Thus, the initial near-zero hardening stage corresponds to the twinning-dominated regime, and since the twinned (and reoriented) regions require higher stresses to slip, the response transitions into a concave upward stress–strain curve.
- For both dog-bone and single-edge notch specimens, the ⟨001⟩ orientation is initially softer than ⟨111⟩. However, due to a higher initial strain-hardening rate, the ⟨001⟩ specimens become harder with increasing deformation. In ⟨111⟩ dog-bone specimens, since the stress–strain curve transitions into a concave upward shape, they ultimately exhibit strength levels comparable to or greater than those of the ⟨001⟩ specimens.
- Compared to dog-bone specimens, both ⟨001⟩ and ⟨111⟩ notched specimens show a notch-strengthening effect, with higher stresses required at the same deformation levels. The stress–strain curves of both ⟨001⟩ dog-bone and single-edge notch specimens are qualitatively similar, exhibiting a nearly concave downward shape. However, the stress–strain curves of ⟨111⟩

dog-bone and single-edge notch specimens differ significantly. In the presence of a notch, the ⟨111⟩ orientation does not exhibit the near-zero hardening stage but instead shows a continuous sub-linear hardening response.

- Comparison of predictions with and without twinning as an active deformation mechanism shows that the response of ⟨001⟩-oriented specimens remains largely unchanged, even though limited twinning may occur in single-edge notch specimens due to the multiaxial stress state. In contrast, deactivating twinning has a significant effect on the response of ⟨111⟩ specimens. Without twinning, both ⟨111⟩-oriented dog-bone and single-edge notch specimens are much harder than the ⟨001⟩ specimens, consistent with the relative Schmid factors associated with these orientations. Additionally, without twinning, both ⟨111⟩-oriented dog-bone and single-edge notch specimens exhibit a sub-linear hardening response.
- The CPFE simulations also accurately capture the experimentally observed notch deformation in both ⟨001⟩- and ⟨111⟩-oriented single-edge notch specimens. For the ⟨001⟩-oriented specimens, the initially semi-circular notch tip flattens and opens symmetrically. In the ⟨111⟩-oriented specimens, the notch tip also flattens, but the flattened edge becomes inclined, resulting in a highly asymmetric overall notch deformation. Predictions for the ⟨111⟩-oriented specimens without twinning show that the notch deformation remains asymmetric, although both the extent of notch tip deformation and the degree of deformation asymmetry are significantly reduced compared to the case with active twinning.
- Although crack nucleation is not explicitly modeled, the predicted distributions of stress measures associated with ductile failure provide insight into crack initiation. For the ⟨001⟩-oriented specimens, with or without twinning, the stress fields are nearly symmetric across the notch, with peak values, especially stress triaxiality, concentrated along the centerline. This suggests the nucleation of a single crack, consistent with experiments. In contrast, the ⟨111⟩-oriented specimens show asymmetric stress distributions, and with twinning, elevated stress triaxiality appears in discrete pockets along the notch periphery. This pattern indicates a propensity for multiple crack nucleation sites, in agreement with experimental observations.

CRediT authorship contribution statement

S. Virupakshi: Writing – original draft, Visualization, Validation, Software, Methodology, Investigation, Formal analysis, Data curation. **X. Zheng:** Writing – review & editing, Visualization, Validation, Methodology, Investigation. **K. Frydrych:** Writing – review & editing, Software, Methodology. **I. Karaman:** Writing – review & editing, Validation, Resources. **A. Srivastava:** Writing – original draft, Validation, Supervision, Resources, Methodology, Funding acquisition, Data curation, Conceptualization. **K. Kowalczyk-Gajewska:** Writing – original draft, Validation, Supervision, Software, Resources, Methodology, Investigation, Funding acquisition, Formal analysis, Data curation, Conceptualization.

Declaration of competing interest

The authors declare that they have no conflict of interest.

## Appendix A. Mesh sensitivity study for the PTVC reorientation scheme

This appendix examines the sensitivity of the PTVC reorientation scheme to mesh size and small perturbations of parameters.

In multiple calculations related to parameter identification using a genetic algorithm, it was observed that the results of the PTVC reorientation procedure are not highly sensitive (in the ergodic sense) to small perturbations of material parameters. For a single Gauss point, even a small variation of material parameters can drastically change the moment during the calculation when the reorientation condition is satisfied, due to the random polling included in the procedure. However, when observing a statistically meaningful number of Gauss points from a given domain, their collective response is not visibly different. Despite the limitation regarding the prediction of morphological features, this is consistent with physical reality, in which the exact location of twin nucleation sites in a single crystal under uniform loading cannot be precisely predicted and is dictated by small-scale fluctuations in the crystal lattice (Huang et al., 2025).

Mesh size influences the size of a single reoriented domain, visible as a red spot in Figs. 4, 7, 9, and 10, which correspond to twinned domains. The reorientation condition is checked at each Gauss point, which then assumes the twin-related orientation. This effect is illustrated in Fig. A.14, where three different meshes – coarse, regular (used in the study in Section 4.1), and dense – are used in the simulations. The overall effect, however, is negligible as long as a statistically meaningful number of elements is used. In Fig. A.15, the stress–strain curves and accumulated slip and twin volume fractions predicted for the gauge area of the sample are compared for three mesh densities. Only slight differences exist between the results for the coarse and regular meshes, while the curves for the regular and dense meshes almost coincide. In Fig. A.16, the influence of mesh size on the predicted
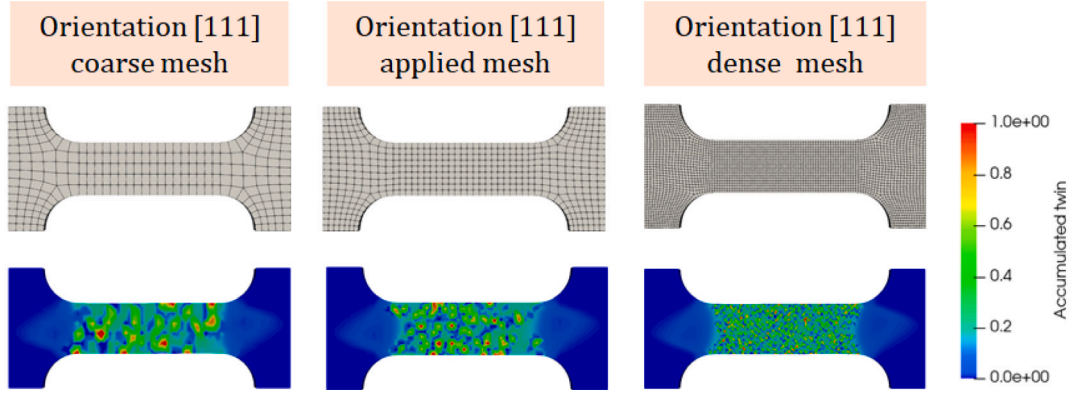
Fig. A.14. Three mesh densities for the dog-bone sample, together with contour plots of accumulated twin at a strain of 0.051, demonstrating the impact of the probabilistic reorientation condition, in which reorientation is performed at the Gauss point level (red spots in the contour maps correspond to reoriented domains). (For interpretation of the references to color in this figure legend, the reader is referred to the web version of this article.)
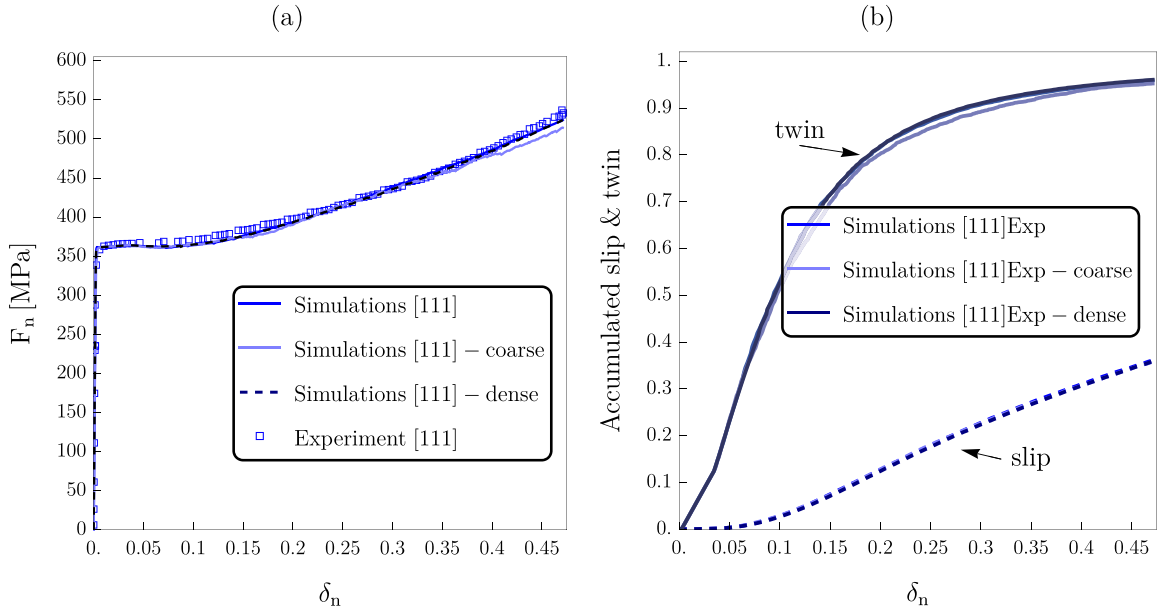

Fig. A.15. (a) Comparison of experimentally obtained and predicted normalized force–displacement (F_n–δ_n) curves for dog-bone specimens with the [111] crystal orientation, subjected to uniaxial tension, using three different mesh densities. (b) Predicted evolution of accumulated slip and twin volume fractions, averaged over the gauge region of the specimen.

notch deformation and the spatial distribution of accumulated twinning is presented. Similar to the dog-bone sample, the notch deformation is not significantly affected when changing from the currently applied mesh to a coarser one. The normalized force–normalized displacement curves and accumulated slip and twin (twin kinetics) predicted for the gauge area of the notch sample (results not shown) show almost no difference between the coarse and regular meshes.

Appendix B. Influence of latent hardening coefficients

Within the identification procedure, the latent hardening coefficients $q^{(\alpha\beta)}$ were assumed to be equal to 1, which was also beneficial from a computational efficiency standpoint. Naturally, the pre-assumed values of these parameters can influence the final results. To assess this effect, calculations were performed for a dog-bone specimen without a notch, oriented along [111], using three alternative values of the latent hardening coefficient: $q = 0$, $q = 1.4$, and a case with latent hardening completely neglected (note that setting $q^{(\alpha\beta)} = 0$ in the formula $h_{rq}^{(\alpha\beta)} = q^{(\alpha\beta)} + (1 - q^{(\alpha\beta)})|\mathbf{n}^r \cdot \mathbf{n}^q|$ does not fully eliminate latent hardening). All other parameters were kept the same.
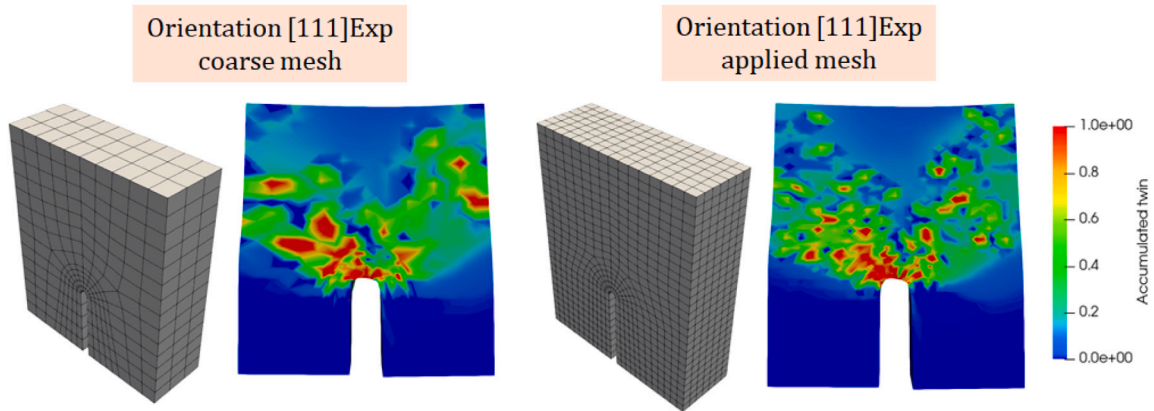
Fig. A.16. Two mesh densities for the notch sample, together with contour plots of accumulated twin at a strain of 0.025, demonstrating the impact of the probabilistic reorientation condition, in which reorientation is performed at the Gauss point level (red spots in the contour maps correspond to reoriented domains). (For interpretation of the references to color in this figure legend, the reader is referred to the web version of this article.)
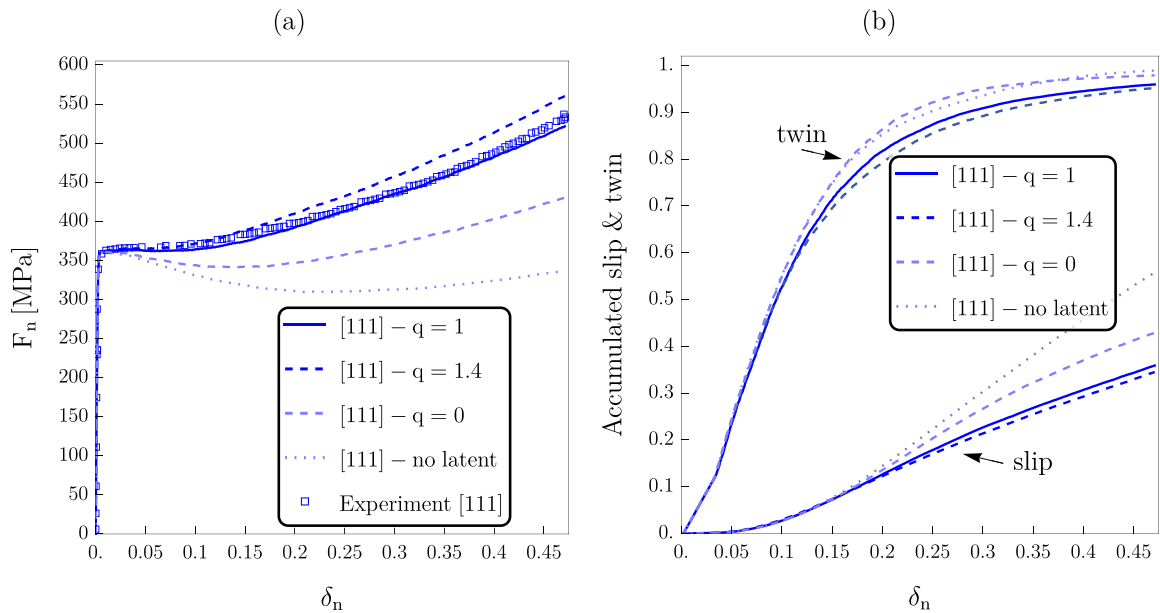

Fig. B.17. Comparison of results obtained with different values of $q = q^{(ss)} = q^{(ts)} = q^{(tt)}$ in Eqs. (9) and (12): (a) normalized force–displacement (F_n–δ_n) curves for a dog-bone specimen with the [111] crystal orientation subjected to uniaxial tension; (b) predicted evolution of accumulated slip and twin volume fractions, averaged over the gauge region of the specimen.

As expected, taking the latent hardening coefficient equal to zero reduced the hardening rate in the stress–strain curve (see Fig. B.17a). The impact on twin kinetics was less pronounced (see Fig. B.17b), although twins accumulated faster when $q = 0$ or when latent hardening was entirely neglected. Regarding slip activity, reducing the latent hardening coefficient increased slip activity at later stages of deformation, when slip primarily occurred in reoriented grains. In contrast, assuming a more physically justified value of q greater than 1 (here $q = 1.4$) did not significantly change the results.

As expected, modifying the latent hardening coefficients $q^{(\alpha\beta)}$ led to a loss of agreement between the simulated stress–strain curves and experimental data, since the parameters were originally identified for $q = 1$. Figs. B.18 and B.19 compare results for a notch specimen with $q = 1$ and $q = 0$. As expected, the response for $q = 0$ is softer than for $q = 1$. In this case, twin kinetics are affected at later stages of the tensile process, and – unlike in the dog-bone specimen without a notch – less twinning is accumulated for $q = 0$.
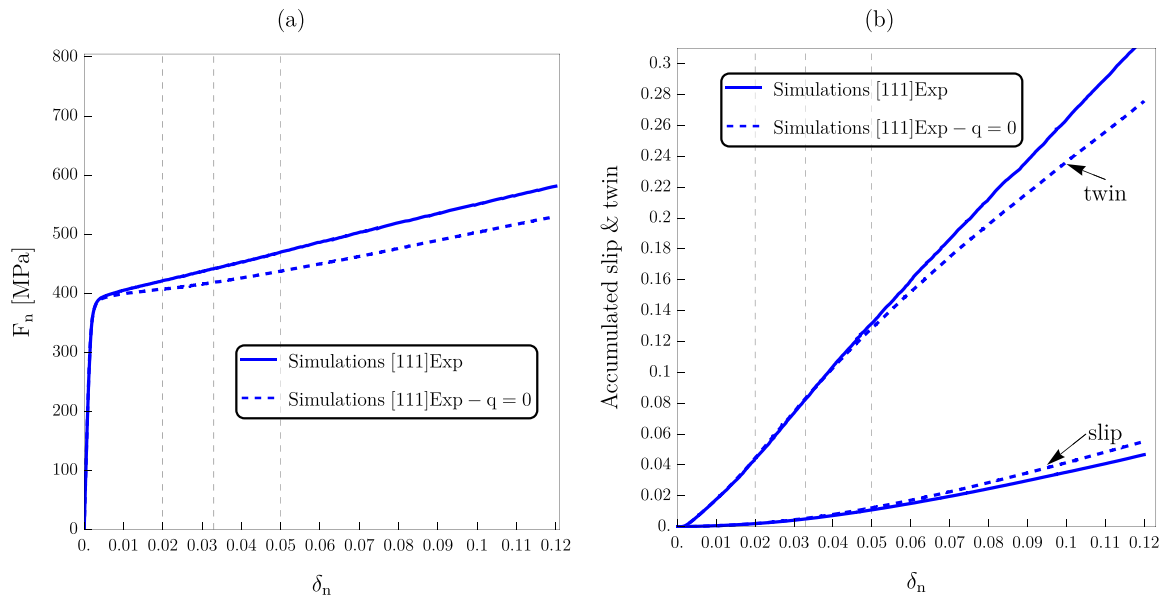
Fig. B.18. Comparison of results obtained with $q = 1$ and $q = 0$ for a notch sample: (a) normalized force–displacement (F_n–δ_n) curves for notch specimens with the [111]Exp crystal orientation subjected to uniaxial tension; (b) predicted evolution of accumulated slip and twin volume fractions, averaged over the gauge region of the notch specimen.
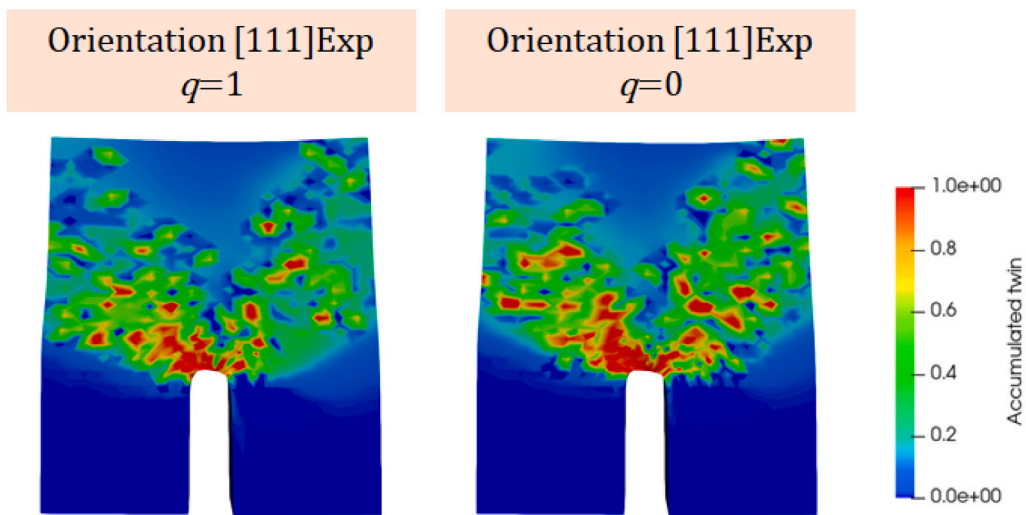
Fig. B.19. Comparison of contour plots of accumulated twin in the notch area at a strain of 0.025 for $q = 1$ and $q = 0$.

Data availability

Data will be made available on request.

References

Adler, P., Olson, G., Owen, W., 1986. Strain hardening of Hadfield manganese steel. Met. Mater. Trans. 17 (10), 1725–1737.

Ardeljan, M., McCabe, R.J., Beyerlein, I.J., Knezevic, M., 2015. Explicit incorporation of deformation twins into crystal plasticity finite element models. Comput. Methods Appl. Mech. Engrg. 295, 396–413. http://dx.doi.org/10.1016/j.cma.2015.07.003.

Asaro, R., Needleman, A., 1985. Overview no. 42 Texture development and strain hardening in rate dependent polycrystals. Acta Metall. 33 (6), 923–953. http://dx.doi.org/10.1016/0001-6160(85)90188-9.

Baweja, S., Joshi, S.P., 2024. Microstructural effects in rate-dependent responses of smooth and notched magnesium bars. Mech. Mater. 189, 104877. http://dx.doi.org/10.1016/j.mechmat.2023.104877, URL: https://www.sciencedirect.com/science/article/pii/S016766362300323X.

Bayraktar, E., Khalid, F., Levaillant, C., 2004. Deformation and fracture behaviour of high manganese austenitic steel. J. Mater. Process. Technol. 147 (2), 145–154.

Canadinc, D., Sehitoglu, H., Maier, H., Niklasch, D., Chumlyakov, Y., 2007. Orientation evolution in Hadfield steel single crystals under combined slip and twinning. Int. J. Solid Struct. 44 (1), 34–50.

Chang, Y., Kochmann, D.M., 2015. A variational constitutive model for slip-twinning interactions in hcp metals: Application to single- and polycrystalline magnesium. Int. J. Plast. 73, 39–61. http://dx.doi.org/10.1016/j.ijplas.2015.03.008, Special Issue on Constitutive Modeling from Micro-Scale to Continuum in Honor of Prof. Frédéric Barlat.

Cheng, Y., Qiao, H., Fu, Y., Xin, Y., He, Q., Huang, X., Chen, G., Wu, P., Liu, Q., 2024. Mechanical anisotropy induced by the competition between twinning and basal slip of AZ31 magnesium alloy under biaxial tension. Int. J. Plast. 178, 104005. http://dx.doi.org/10.1016/j.ijplas.2024.104005.

Cheng, J., Shen, J., Mishra, R.K., Ghosh, S., 2018. Discrete twin evolution in Mg alloys using a novel crystal plasticity finite element model. Acta Mater. 149, 142–153. http://dx.doi.org/10.1016/j.actamat.2018.02.032.

Chester, S.A., Bernier, J.V., Barton, N.R., Balogh, L., Clausen, B., Edmiston, J.K., 2016. Direct numerical simulation of deformation twinning in polycrystals. Acta Mater. 120, 348–363. http://dx.doi.org/10.1016/j.actamat.2016.08.054.

Chin, G.Y., Hosford, W.F., Mendorf, D.R., Taylor, G.I., 1969. Accommodation of constrained deformation in f. c. c. metals by slip and twinning. Proc. R. Soc. A 309 (1499), 433–456. http://dx.doi.org/10.1098/rspa.1969.0051.

Clausen, B., Lorentzen, T., Leffers, T., 1998. Self-consistent modelling of the plastic deformation of f.c.c. polycrystals and its implications for diffraction measurements of internal stresses. Acta Mater. 46 (9), 3087–3098. http://dx.doi.org/10.1016/S1359-6454(98)00014-7.

Dastur, Y., Leslie, W., 1981. Mechanism of work hardening in Hadfield manganese steel. Metall. Trans. A 12 (5), 749–759.

Ding, Z., Dong, L., Huang, Q., Guo, J., Tian, R., Yan, F., 2024. Formation of intracrystalline deformation twins in austenitic Mn-steel at the early stage of plastic deformation. J. Mater. Sci. Technol. 197, 129–138. http://dx.doi.org/10.1016/j.jmst.2024.01.049.

Dittmann, J., Wulfinghoff, S., 2023. Efficient numerical strategies for an implicit volume fraction transfer scheme for single crystal plasticity including twinning and secondary plasticity on the example of magnesium. Internat. J. Numer. Methods Engrg. 124 (21), 4718–4739. http://dx.doi.org/10.1002/nme.7329.

Efstathiou, C., Sehitoglu, H., 2010. Strain hardening and heterogeneous deformation during twinning in Hadfield steel. Acta Mater. 58 (5), 1479–1488.

El Kadiri, H., Oppedal, A., 2010. A crystal plasticity theory for latent hardening by glide twinning through dislocation transmutation and twin accommodation effects. J. Mech. Phys. Solids 58 (4), 613–624. http://dx.doi.org/10.1016/j.jmps.2009.12.004.

Frydrych, K., Kowalczyk-Gajewska, K., 2018. Grain refinement in the equal channel angular pressing process: simulations using the crystal plasticity finite element method. Modelling Simul. Mater. Sci. Eng. 26 (6), 065015. http://dx.doi.org/10.1088/1361-651X/aad46d.

Frydrych, K., Libura, T., Kowalewski, Z., Maj, M., Kowalczyk-Gajewska, K., 2021. On the role of slip, twinning and detwinning in magnesium alloy AZ31B sheet. Mater. Sci. Eng. 813, http://dx.doi.org/10.1016/j.msea.2021.141152.

Frydrych, K., Maj, M., Urbański, L., Kowalczyk-Gajewska, K., 2020. Twinning-induced anisotropy of mechanical response of AZ31B extruded rods. Mater. Sci. Eng. 771, 138610. http://dx.doi.org/10.1016/j.msea.2019.138610.

Gürol, U., Kurnaz, S.C., 2020. Effect of carbon and manganese content on the microstructure and mechanical properties of high manganese austenitic steel. J. Min. Met. Sect. Met. 56 (2), 171–182. http://dx.doi.org/10.2298/JMMB191111009G.

Havel, D., 2017. Austenitic Manganese Steel: A Complete Overview. Technical Report, Columbia Steel Casting Co., Inc.

Havlíček, P., Bušová, K., 2012. Experience with explosive hardening of railway frogs from Hadfield steel. In: METAL 2012 - Conference Proceedings, 21st International Conference on Metallurgy and Materials. TANGER Ltd.

Herbig, M., Kuzmina, M., Haase, C., Marceau, R.K., Gutiérrez-Urrutia, I., Haley, D., Molodov, D.A., Choi, P., Raabe, D., 2015. Grain boundary segregation in Fe–Mn–C twinning-induced plasticity steels studied by correlative electron backscatter diffraction and atom probe tomography. Acta Mater. 83, 37–47. http://dx.doi.org/10.1016/j.actamat.2014.09.041.

Hill, R., Rice, J., 1972. Constitutive analysis of elastic-plastic crystals at arbitrary strain. J. Mech. Phys. Solids 20 (6), 401–413. http://dx.doi.org/10.1016/0022-5096(72)90017-8.

Hollenweger, Y., Kochmann, D.M., 2022. An efficient temperature-dependent crystal plasticity framework for pure magnesium with emphasis on the competition between slip and twinning. Int. J. Plast. 159, 103448. http://dx.doi.org/10.1016/j.ijplas.2022.103448.

Huang, C., Gao, B., Zhou, N., Xin, R., Tang, S., Elkhodary, K., 2022. Enabling high-fidelity twin pattern prediction in polycrystals — A mesoscale grain boundary plasticity model. Int. J. Plast. 148, 103121. http://dx.doi.org/10.1016/j.ijplas.2021.103121.

Huang, J., Lei, M., Yang, G., Wen, B., 2025. Twinning induced by asymmetric shear response. Int. J. Plast. 185, 104226. http://dx.doi.org/10.1016/j.ijplas.2024.104226.

Hutchinson, B., Ridley, N., 2006. On dislocation accumulation and work hardening in Hadfield steel. Scr. Mater. 55 (4), 299–302.

Kalidindi, S.R., 1998. Incorporation of deformation twinning in crystal plasticity models. J. Mech. Phys. Solids 46 (2), 267–290. http://dx.doi.org/10.1016/S0022-5096(97)00051-3.

Kalidindi, S.R., 2001. Modeling anisotropic strain hardening and deformation textures in low stacking fault energy fcc metals. Int. J. Plast. 17 (6), 837–860. http://dx.doi.org/10.1016/S0749-6419(00)00071-1.

Karaman, I., Sehitoglu, H., Beaudoin, A., Chumlyakov, Y., Maier, H., Tomé, C., 2000a. Modeling the deformation behavior of Hadfield steel single and polycrystals due to twinning and slip. Acta Mater. 48 (9), 2031–2047. http://dx.doi.org/10.1016/S1359-6454(00)00051-3.

Karaman, I., Sehitoglu, H., Chumlyakov, Y., Maier, H., Kireeva, I., 2001a. Extrinsic stacking faults and twinning in Hadfield manganese steel single crystals. Scr. Mater. 44 (2), 337–343.

Karaman, I., Sehitoglu, H., Chumlyakov, Y.I., Maier, H.J., Kireeva, I.V., 2001b. The effect of twinning and slip on the Bauschinger effect of Hadfield steel single crystals. Met. Mater. Trans. 32A, 695–706.

Karaman, I., Sehitoglu, H., Gall, K., Chumlyakov, Y., 1998. On the deformation mechanisms in single crystal Hadfield manganese steels. Scr. Mater. 38 (6), 1009–1015.

Karaman, I., Sehitoglu, H., Gall, K., Chumlyakov, Y., Maier, H., 2000b. Deformation of single crystal Hadfield steel by twinning and slip. Acta Mater. 48 (6), 1345–1359.

Kaushik, V., Narasimhan, R., Mishra, R., 2014a. Experimental study of fracture behavior of magnesium single crystals. Mater. Sci. Eng. 590, 174–185.

Kaushik, V., Narasimhan, R., Mishra, R.K., 2014b. Finite element simulations of notch tip fields in magnesium single crystals. Int. J. Fract. 189, 195–216.

Korelc, J., 2002. Multi-language and multi-environment generation of nonlinear finite element codes. Eng. Comput. 18, 312–327.

Korelc, J., Stupkiewicz, S., 2014. Closed-form matrix exponential and its application in finite-strain plasticity. Internat. J. Numer. Methods Engrg. 98 (13), 960–987. http://dx.doi.org/10.1002/nme.4653.

Kowalczyk-Gajewska, K., 2010. Modelling of texture evolution in metals accounting for lattice reorientation due to twinning. Eur. J. Mech. A Solids 29 (1), 28–41. http://dx.doi.org/10.1016/j.euromechsol.2009.07.002.

Kowalczyk-Gajewska, K., 2011. Micromechanical modelling of metals and alloys of high specific strength. In: IFTR Reports 1/2011. Warszawa, pp. 1–299.

Kowalczyk-Gajewska, K., 2013. Crystal plasticity models accounting for twinning. Comput. Methods Mater. Sci. 13, 436–451.

Kucharski, S., Stupkiewicz, S., Petryk, H., 2014. Surface pile-up patterns in indentation testing of Cu single crystals. Exper. Mech. 54 (6), 957–969. http://dx.doi.org/10.1007/s11340-014-9883-1.

Lebensohn, R., Tomé, C., 1993. A self-consistent anisotropic approach for the simulation of plastic deformation and texture development of polycrystals: Application to zirconium alloys. Acta Met. Mater. 41 (9), 2611–2624. http://dx.doi.org/10.1016/0956-7151(93)90130-K.

Lindroos, M., Cailletaud, G., Laukkanen, A., Kuokkala, V.-T., 2018. Crystal plasticity modeling and characterization of the deformation twinning and strain hardening in Hadfield steels. Mater. Sci. Eng. 720, 145–159. http://dx.doi.org/10.1016/j.msea.2018.02.028.

Liu, C., Roters, F., Raabe, D., 2023. Finite strain crystal plasticity-phase field modeling of twin, dislocation, and grain boundary interaction in hexagonal materials. Acta Mater. 242, 118444. http://dx.doi.org/10.1016/j.actamat.2022.118444.

Liu, Y., Wei, Y., 2014. A polycrystal based numerical investigation on the temperature dependence of slip resistance and texture evolution in magnesium alloy AZ31B. Int. J. Plast. 55, 80–93. http://dx.doi.org/10.1016/j.ijplas.2013.09.011.

Mànik, T., Asadkandi, H., Holmedal, B., 2022. A robust algorithm for rate-independent crystal plasticity. Comput. Methods Appl. Mech. Engrg. 393, http://dx.doi.org/10.1016/j.cma.2022.114831.

Meyers, M., Vöhringer, O., Lubarda, V., 2001. The onset of twinning in metals: A constitutive description. Acta Mater. 49 (19), 4025–4039. http://dx.doi.org/10.1016/S1359-6454(01)00300-7, URL: https://www.sciencedirect.com/science/article/pii/S1359645401003007.

Mo, H., Liu, G., Mao, Y., Shen, Y., Wang, J., 2022. Dual-interface model for twinning in the coupled crystal plasticity finite element – Phase field method. Int. J. Plast. 158, 103441. http://dx.doi.org/10.1016/j.ijplas.2022.103441.

Okechukwu, C., Dahunsi, O.A., Oke, P.K., Oladele, I.O., Dauda, M., 2018. Development of hardfaced crusher jaws using ferro-alloy hardfacing inserts and low carbon steel substrate. J. Tribol 18, 20–39.

Prasad, N.S., Narasimhan, R., Suwas, S., 2017. Effects of lattice orientation and crack tip constraint on ductile fracture initiation in Mg single crystals. Int. J. Plast. 97, 222–245. http://dx.doi.org/10.1016/j.ijplas.2017.06.004, URL: https://www.sciencedirect.com/science/article/pii/S0749641917302085.

Proust, G., Tomé, C., Kaschner, G., 2007. Modeling texture, twinning and hardening evolution during deformation of hexagonal materials. Acta Mater. 55 (6), 2137–2148. http://dx.doi.org/10.1016/j.actamat.2006.11.017.

Qiao, H., Barnett, M., Wu, P., 2016. Modeling of twin formation, propagation and growth in a Mg single crystal based on crystal plasticity finite element method. Int. J. Plast. 86, 70–92. http://dx.doi.org/10.1016/j.ijplas.2016.08.002.

Qiao, H., Guo, X., Hong, S., Wu, P., 2017. Modeling of 10-12-10-12 secondary twinning in pre-compressed Mg alloy AZ31. J. Alloys Compd. 725, 96–107. http://dx.doi.org/10.1016/j.jallcom.2017.07.133, URL: https://www.sciencedirect.com/science/article/pii/S0925838817324982.

Raghavan, K., Sastri, A., Marcinkowski, M., 1969. Nature of the work-hardening behavior in hadfields manganese steel. Trans. Met. Soc. AIME 245 (7), 1569–1575.

Rezaee-Hajidehi, M., aw Sadowski, P., Stupkiewicz, S., 2022. Deformation twinning as a displacive transformation: Finite-strain phase-field model of coupled twinning and crystal plasticity. J. Mech. Phys. Solids 163, 104855. http://dx.doi.org/10.1016/j.jmps.2022.104855.

Sahoo, S.K., Biswas, S., Toth, L.S., Gautam, P., Beausir, B., 2020. Strain hardening, twinning and texture evolution in magnesium alloy using the all twin variant polycrystal modelling approach. Int. J. Plast. 128, 102660. http://dx.doi.org/10.1016/j.ijplas.2020.102660.

Sahoo, S.K., Toth, L.S., Biswas, S., 2019. An analytical model to predict strain-hardening behaviour and twin volume fraction in a profoundly twinning magnesium alloy. Int. J. Plast. 119, 273–290. http://dx.doi.org/10.1016/j.ijplas.2019.04.007.

Sahu, V.K., Chakraborty, P., Yadava, M., Gurao, N.P., 2024. Micro-mechanisms of anisotropic deformation in the presence of notch in commercially pure titanium: An in-situ study with CPFEM simulations. Int. J. Plast. 177, http://dx.doi.org/10.1016/j.ijplas.2024.103985.

Selvarajou, B., Kondori, B., Benzerga, A.A., Joshi, S.P., 2016. On plastic flow in notched hexagonal close packed single crystals. J. Mech. Phys. Solids 94, 273–297. http://dx.doi.org/10.1016/j.jmps.2016.04.023.

Shen, S., Xie, P., Wu, C., Luo, J., haifeng Ye, Chen, J., 2024. Cross-slip of extended dislocations and secondary deformation twinning in a high-Mn TWIP steel. Int. J. Plast. 175, 103922. http://dx.doi.org/10.1016/j.ijplas.2024.103922.

Simo, J.C., Hughes, T.J.R., 1998. Computational Inelasticity. Springer.

Srivastava, A., Needleman, A., 2015. Effect of crystal orientation on porosity evolution in a creeping single crystal. Mech. Mater. 90, 10–29. http://dx.doi.org/10.1016/j.mechmat.2015.01.015, URL: https://www.sciencedirect.com/science/article/pii/S0167663615000228. Proceedings of the IUTAM Symposium on Micromechanics of Defects in Solids.

Staroselsky, A., Anand, L., 1998. Inelastic deformation of polycrystalline face centered cubic materials by slip and twinning. J. Mech. Phys. Solids 46 (4), 671–696. http://dx.doi.org/10.1016/S0022-5096(97)00071-9.

Staroselsky, A., Anand, L., 2003. A constitutive model for hcp materials deforming by slip and twinning: application to magnesium alloy AZ31B. Int. J. Plast. 19 (10), 1843–1864. http://dx.doi.org/10.1016/S0749-6419(03)00039-1.

Subramanyam, D., Swansiger, A., Avery, H., 1990. Austenitic manganese steels. In: ASM Handbook Committee (Ed.), Properties and Selection: Irons, Steels, and High-Performance Alloys. Vol. 1, ASM International, Materials Park, OH, pp. 822–840.

Szczerba, M., Bajor, T., Tokarski, T., 2004. Is there a critical resolved shear stress for twinning in face-centred cubic crystals? Phil. Mag. 84 (3–5), 481–502. http://dx.doi.org/10.1080/14786430310001612175.

Tomé, C., Lebensohn, R., Kocks, U., 1991. A model for texture development dominated by deformation twinning: Application to zirconium alloys. Acta Met. Mater. 39 (11), 2667–2680. http://dx.doi.org/10.1016/0956-7151(91)90083-D.

Wang, H., Wu, P., Wang, J., Tome, C., 2013. A crystal plasticity model for hexagonal close packed (HCP) crystals including twinning and de-twinning mechanisms. Int. J. Plast. 49, 36–52. http://dx.doi.org/10.1016/j.ijplas.2013.02.016.

Wong, S.L., Madivala, M., Prahl, U., Roters, F., Raabe, D., 2016. A crystal plasticity model for twinning- and transformation-induced plasticity. Acta Mater. 118, 140–151. http://dx.doi.org/10.1016/j.actamat.2016.07.032.

Yaghoobi, M., Allison, J.E., Sundararaghavan, V., 2020. Multiscale modeling of twinning and detwinning behavior of HCP polycrystals. Int. J. Plast. 127, 102653. http://dx.doi.org/10.1016/j.ijplas.2019.102653.

Yaghoobi, M., Chen, Z., Murphy-Leonard, A.D., Sundararaghavan, V., Daly, S., Allison, J.E., 2022. Deformation twinning and detwinning in extruded Mg-4Al: In-situ experiment and crystal plasticity simulation. Int. J. Plast. 155, 103345. http://dx.doi.org/10.1016/j.ijplas.2022.103345.

Zhang, J., Joshi, S.P., 2012. Phenomenological crystal plasticity modeling and detailed micromechanical investigations of pure magnesium. J. Mech. Phys. Solids 60, 945–972.

Zheng, X., Karaman, I., Srivastava, A., 2025. Interaction of deformation twinning and crack growth in single crystals of an austenitic manganese steel. Mater. Sci. Eng. 924, 147779. http://dx.doi.org/10.1016/j.msea.2024.147779.